

Article

Integrating Hydrokinetic Energy into Hybrid Renewable Energy System: Optimal Design and Comparative Analysis

Gbalimene Richard Ileberi and Pu Li * 

Group of Process Optimization, Institute of Automation and Systems Engineering,
Ilmenau University of Technology, 98693 Ilmenau, Germany; gbalimene-richard.ileberi@tu-ilmenau.de

* Correspondence: pu.li@tu-ilmenau.de

Abstract: Renewable energy resources and energy efficiency measures are effective means of curtailing CO₂ emissions. Solar and wind technologies have been mostly developed to meet the energy demand of off-grid remote areas or locations without grid connections. However, it is well-known that the power generation of these resources is affected by daily fluctuations and seasonal variability. One way to mitigate such an effect is to incorporate hydrokinetic resources into the energy system, which has not been well investigated yet. Therefore, this study examines the prospects of designing a hybrid system that integrates hydrokinetic energy to electrify an off-grid area. Hydrokinetic energy generation depends on water flow velocity (WFV). We estimate WFV by a model-based approach with geographical and weather data as inputs. Together with the models of the other components (wind turbine, PV panel, battery, and diesel generator) in the micro-grid, an optimization problem is formulated with the total net present cost and the cost of energy as performance criteria. A genetic algorithm (GA) is used to solve this problem for determining an optimal system configuration. Applying our approach to a small community in Nigeria, our findings show that the flow velocity of a nearby river ranges between 0.017 and 5.12 m/s, with a mean velocity of 0.71 m/s. The resulting optimal micro-grid consists of 320 kW of PV, 120 units of 6.91 kWh batteries, 2 (27 kW) hydrokinetic turbines, an 120 kW converter, zero wind turbines, and a 100 kW diesel generator. As a result, the total energy generated will be 471,743 kWh/year, of which 12% emanates from hydrokinetic energy. The total net present cost, the cost of energy, and the capital cost are USD 1,103,668, 0.2841 USD/kWh, and USD 573,320, respectively.



Citation: Ileberi, G.R.; Li, P.

Integrating Hydrokinetic Energy into Hybrid Renewable Energy System: Optimal Design and Comparative Analysis. *Energies* **2023**, *16*, 3403. <https://doi.org/10.3390/en16083403>

Academic Editors: Helena M. Ramos and Chirag Trivedi

Received: 13 February 2023

Revised: 3 April 2023

Accepted: 10 April 2023

Published: 12 April 2023



Copyright: © 2023 by the authors. Licensee MDPI, Basel, Switzerland. This article is an open access article distributed under the terms and conditions of the Creative Commons Attribution (CC BY) license (<https://creativecommons.org/licenses/by/4.0/>).

Keywords: hydrokinetic energy; flow velocity model; net present cost; hybrid renewable energy system; optimal design

1. Introduction

It is reported that around 860 million people worldwide lack access to electricity, and more than two-thirds emanate from Africa [1]. Furthermore, the global population projection indicates an increase of 2 billion people in the next 30 years; this will trigger a rise in energy demand by 1.3% annually up to 2040 [2,3]. Presently, a significant share of energy production comes from fossil fuel sources, such as coal, oil, and gas. With global oil reserves dwindling and the adverse climatic impact attributed to continuous energy generation from these conventional means, a more sustainable and environmentally-friendly approach is needed to meet energy demand that involves integrating renewable energy sources (RES) into the mix.

Renewable energy technologies have recently gained momentum, as seen in the RES share, which increased from 24% in 2000 to 44% of the total power capacity at the start of 2016 [4]. For the first time in the European Union, in 2021, 38% of end-user electricity was supplied by renewable resources, whereas 37% was supplied by fossil fuels [5]. Amongst other RES, the current trend shows that solar and wind resources are gradually becoming the major players in the quest for clean and sustainable energy. Most

studies are geared towards this direction [6] for off-grid and on-grid applications in the area of health centers [7–9], educational facilities [10–12], telecommunication stations [13–15], residential households [16–18], and rural communities [19–22]. Moreover, about 100 GW and 60 GW of solar and wind power projects were, respectively, completed worldwide in 2019 [23].

Beside wind and solar, other forms of RES are predicted to increase as envisaged by the International Energy Agency, which forecasted that, between 2019–2024, hydropower will remain the primary source and the capacities of bioenergy and geothermal will increase by 34% and 28%, respectively [24]. Moreover, a resource assessment study conducted by the EPRI [25] indicates that the potential of rivers in the US for harnessing hydrokinetic power is estimated at 1381 TW h/y. The flow velocity is significant in evaluating the hydrokinetic energy potential of rivers. The higher the flow velocity, the higher the possibility of generating sufficient energy. Therefore, studies have been conducted on flow velocities and energy potentials. Mean flow velocities for some studied rivers in the US show values ranging between 0.46 and 1.01 m/s [26]. Similarly, the authors in [27] indicate that the discharge in some rivers across Nigeria has average discharge values from 2.2 to 6635 m³/s, and the hydrokinetic potential in the northern part of the country is estimated at 66.18 MW, while that of the southern part is 42.97 MW. Chen et al. [28] observed that the discharge at the Yangtze River in China has an annual average of 3.0×10^4 m³/s. The authors in [29] proposed a flow velocity model for assessing the available hydrokinetic energy in Amazon in Brazil. The authors concluded that the highest and lowest average velocities in the Amazon River were 2.27 m/s and 0.735 m/s, respectively, and the energy potential ranges between 0.1 and 1488.6 kW. In comparison to meteorological data, which are readily available and used for solar and wind energy applications, there is a paucity of information for a worldwide database that evaluates the flow velocity and energy potential of each river network [30], hence, limiting the application of hydrokinetic power. Moreover, the predominance of hydropower, due to its predictability, high efficiency, and high energy output, has made hydrokinetic power less of a focus. However, rural and remote areas without a grid connection can benefit from clean, safe, and sustainable energy emanating from free-flowing water [31].

Hybrid renewable energy systems (HRES) as a micro-grid have been extensively studied in recent years. A techno-economic feasibility study was made by simulating two different configurations (PV/battery and diesel/battery) to supply the load demand of a mobile station, where a net savings of 59.6% in the net present cost for the PV/battery configuration is obtainable [14]. A solar–wind power on-grid system was proposed for a region in Columbia [32], showing that the optimal system configuration comprises 441 kW PV and three (1.5 MW) wind turbines (WTs), and the net present cost is USD 11.8 million. In Sub-Saharan Africa, a 100% off-grid renewable energy supply system was investigated [33], resulting in an optimal system architecture with an 81.8 kW PV array and a 15 kW biogas generator. Oviroh and Jen [34] proposed a PV-diesel system for a load range of 4 kW to 8 kW and the results showed an optimal LCOE range between 0.156/kWh and 0.172/kWh for an 8 kW load. Similar related studies were conducted regarding HRES with case study applications in India, the United Kingdom, Nigeria, Oman, Egypt, South Africa, Brazil, Namibia, and Bangladesh [35–49]. These studies mainly focused on PV and wind systems as renewable energy generating sources, battery and hydrogen storage as the storage component, and diesel generators as the backup source. However, hydrokinetic energy sources as a component of an HRES were not considered.

Hydrokinetic energy is a form of renewable energy extractable from lakes, waves, rivers, tidal currents, ocean currents, and other water courses. The technology involves converting the kinetic energy of flowing water to electric power using a hydrokinetic turbine (HKT). The hydrokinetic power (HKP) obtainable from a river channel is a function of the density of water, the cross-sectional area of the flowing river (or the swept area of the turbine), and the velocity of water [31]. In addition, temporal and spatial flow analysis needs to be conducted to predict the power of a given river [50]. Nevertheless, the velocity

of the flowing water is crucial, since the power increases with the velocity cubed. Unlike hydropower, which requires dam construction for a potential head, there is little or 'zero head' needed in HKP generation [51]. Hence the financial burden of constructing a dam or reservoir is avoided, provided there is a sufficiently high flow velocity.

As hydrokinetic energy gradually receives attention, available studies in this area have focused on modeling and turbine design [52], HKT enhancement techniques [51], turbine selection [26], and energy conversion mechanisms and technology [31,50]. For a holistic approach to hydrokinetic energy utilization, the research focus should encompass turbine selection and enhancement, energy conversion efficiency, environmental impacts, and assessment studies [31]. A few recent studies considered resource assessment and potential prospects of hydrokinetic technology [27,53–55], but not in the context of a HRES. Moreover, the authors in [56–60] incorporated hydrokinetic energy in the HRES sizing. John et al. [56] considered a hydrokinetic–PV–battery standalone system for tropical climate conditions. The authors obtained an optimum system configuration with 5 HKTs. The HOMER software was utilized to perform a techno-economic analysis of a micro-hydro system in a rural area in eastern India [57]. The result shows that the optimal configuration consists of 24 HKTs and 187 batteries. The authors in [58] investigated the techno-economic feasibility of an off-grid integrated solar/wind/hydrokinetic plant for the cogeneration of electricity and hydrogen to supply a remote community. The result shows that the TNPC and LCOE are USD 333,074 and 0.1155 USD/kWh, respectively. In the same vein, Islam et al. [59] performed a techno-economic optimization of a zero-emission energy system for a coastal community in Newfoundland, Canada. The authors revealed that integrating hydro into a PV/wind/PHS system reduces the cost of energy by 58%. Moreover, the economics of a hydrokinetic turbine for off-grid application were investigated in Ethiopia [60]. The findings show that HKT technology is an economically and technically viable option for off-grid electrification. The studies described so far utilized direct, observed, or measured flow velocities from the closest hydrological stations for their assessment and optimal sizing applications. However, measurements of direct flow velocities are not feasible in many real cases, due to diverse reasons, ranging from high financial cost to the difficulty of access to study area [61]. Therefore, we propose a model-based approach to evaluate flow velocities for a given river based on the meteorological, land use, and soil conditions. We then optimize and evaluate the potential of utilizing hydrokinetic energy, as a component of a hybrid renewable energy system for off-grid rural electrification.

The present study investigates the prospects of integrating hydrokinetic energy into a HRES for an off-grid application. The framework of this study is illustrated in Figure 1. Wind and solar data for different locations are readily available from NASA, NREL, and the European Commission, etc., but flow velocities for a given river network, especially in developing countries, are still challenging [62]. Therefore, based on the fundamental water cycle mechanism, we at first perform a detailed modeling to estimate water velocity relating to precipitation and runoff for a given river basin. Based on the flow velocities estimated, an off-grid HRES model incorporating HKT, WT, PV, battery storage, and a diesel generator is then developed. The battery is used as a backup when the renewable energy sources are insufficient to meet the required load demand. The total net present costs for installing and operating the system over its lifetime and the cost of energy are used as the performance criteria, respectively. A genetic algorithm (GA) is employed to determine the optimal system design. The energy supply for a community in the south of Nigeria is taken as a case study. Based on the data from the studied area, the results shows a significant contribution from the hydrokinetic energy from a nearby river.

The rest of the paper is organized as follows. Section 2 provides the model to estimate the flow velocity. Section 3 presents the off-grid HRES modeling and economic criteria for optimal design. The optimization problem is formulated, and the solution approach is discussed, in Section 4. A breakdown of the case study and component specification are

given in Section 5. The computation results are presented in Section 6, while the conclusion is given in Section 7.

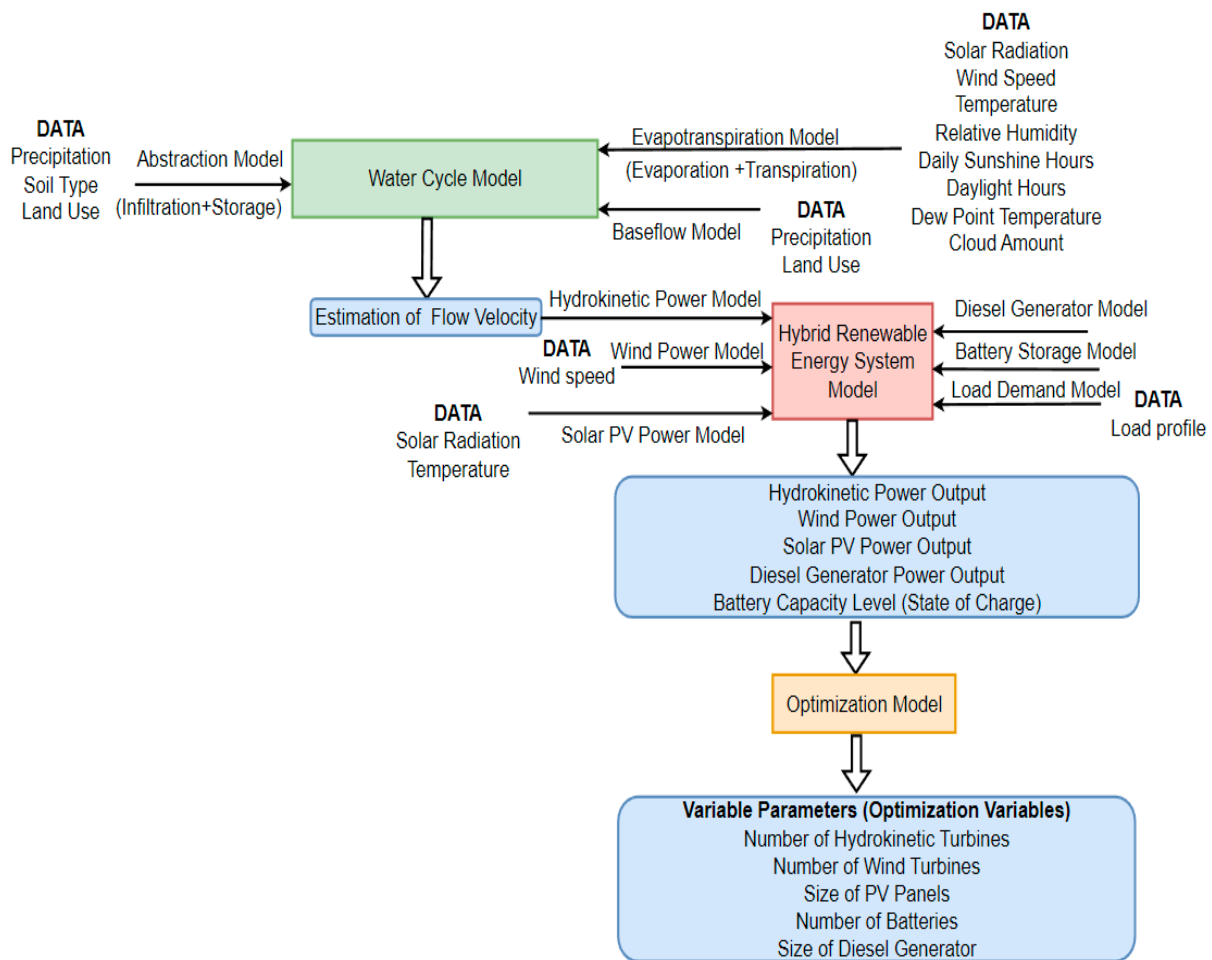


Figure 1. Proposed framework of integrating hydrokinetic power into HRES.

2. Evaluation of Flow Velocity

A river basin can be defined as an open channel with a free surface and modeled as a water cycle compartment. The cycle entails all activities relating to the continuous utilization of water, such as irrigation, land management, crop growth, reservoir routine, etc. To evaluate the flow velocity, it is necessary to model the hydrological process of water transportation. Depending on the application area, the output depends on precipitation, evapotranspiration, soil water content, surface runoff, evaporation from the reservoir, and sediment yield. From Figure 2, precipitation in the form of rainfall hits the Earth’s surface, and, depending on the surface and the elevation of that location, some precipitation infiltrates into the ground, some remains on that surface, while some runs to the stream or river. In addition, some rainfall evaporates to the air and is transpired through plants.

The fundamental governing equation for a water stream can be derived by the water balance that depicts the rainfall-runoff relationship given as [63], as follows:

$$Q^{RS} = P - L \tag{1}$$

where Q^{RS} is the quick or direct runoff to a river or stream, P is the precipitation or rainfall, and L is the total water loss. This loss can result from infiltration (to soil moisture and ground water), evaporation, transpiration, and surface storage [63]. Due to these losses, Equation (1) gives [63]:

$$Q^{RS} = P - I - E - T - S \tag{2}$$

where I is the infiltration, E is the evaporation, T is transpiration, and S is the surface storage. Evaporation and transpiration can be combined as evapotranspiration. Furthermore, infiltration and surface storage can be cumulatively estimated as abstraction. This implies that Equation (2) can also be expressed as follows:

$$Q^{RS} = P - F_a - E_a \quad (3)$$

where F_a is the cumulative abstraction and E_a is the evapotranspiration.

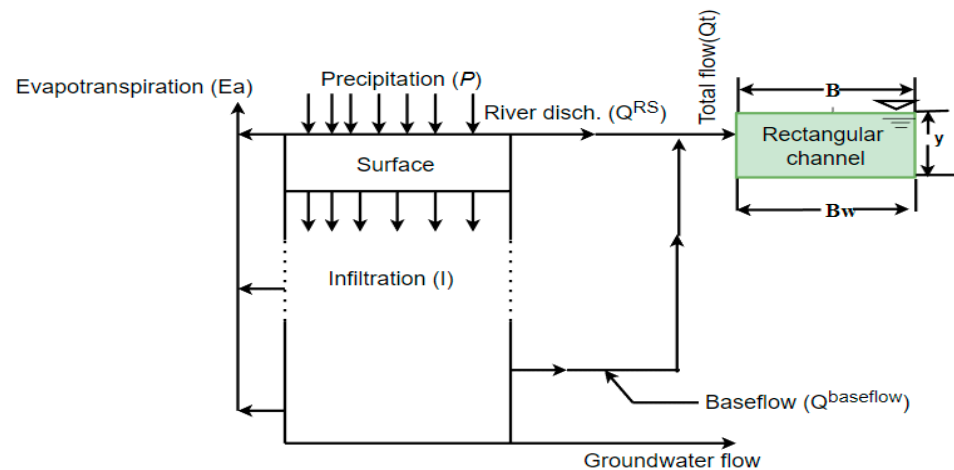


Figure 2. Transportation process of the water cycle [63].

2.1. Estimation of Cumulative Abstraction

The cumulative abstraction can be estimated by using the curve number (CN) of the soil conservation service (SCS) method [64]. It estimates the abstraction as a function of precipitation, soil cover, and land use, as follows:

$$F_a = \begin{cases} \frac{S(P - I_a)}{(P - I_a + S)}, & P \geq I_a \\ 0, & \text{otherwise} \end{cases} \quad (4)$$

where I_a represents the initial abstraction which accounts for infiltration and surface storage, and S is the retention parameter. I_a is commonly approximated as $0.2 S$. S is a measure of the location ability to abstract and retain precipitation. It varies spatially with changes in soil and land use and temporarily due to soil water content, and can be calculated by [65]:

$$S = 25.4 \left(\frac{1000}{CN} - 10 \right) \quad (5)$$

where CN is the curve number that varies from 1 to 100. CN is a function of the soil type, land use, and antecedent moisture condition (AMC). It can be found in the TR-55 table or calculated as a composite CN [66]. As seen in Table 1, AMC is categorized into three levels depending on five days of antecedent rainfall: I (dry season), II (normal or average condition), and III (wet season) [67].

Table 1. AMC classification.

AMC Level	Total 5-Day Antecedent Rainfall (P) (mm)	
	Dry season	Wet season
I	$P < 13$	$P < 36$
II	$13 \leq P \leq 28$	$36 \leq P \leq 53$
III	$P > 28$	$P > 53$

The CN Table provides only the curve number for the values of AMC II (referred to as CN_2). The other categories of the curve number can be calculated as follows [67]:

$$CN_1 = \frac{CN_2}{2.2754 - 0.012754CN_2} \quad (6)$$

$$CN_3 = \frac{CN_2}{0.430 + 0.0057CN_2} \quad (7)$$

2.2. Estimation of the Evapotranspiration

The evapotranspiration can be modeled based on the complementary relation of the modified Penman [68] and Priestley–Taylor [69] equation. This relationship, as defined by the modified advection–aridity method, evaluates evapotranspiration as follows [70]:

$$E_a = (2 \alpha_e - 1) \frac{\Delta}{\Delta + \gamma} \frac{R_n + M}{l} - \frac{\gamma}{\Delta + \gamma} f(U_2)(e_s - e_a) \quad (8)$$

where E_a is the evapotranspiration (mm/d), α_e is the modified Priestley–Taylor parameter taken as 1.26 [69], Δ is the slope of the saturated vapor pressure curve at air temperature (kPa/°C), γ is the psychrometric constant (kPa/°C), R_n is the net radiation (MJ/m²/d), M is the advection energy (MJ/m²/d), l is the latent heat of vaporization (MJ/kg), $f(U_2)$ is a linear approximated wind function relating to the wind speed (m/s) measured at 2 m height, e_s is the saturated vapor pressure (kPa), and e_a is the vapor pressure (kPa).

The slope of the saturated vapor curve can be evaluated by the following [71]:

$$\Delta = \frac{4098 \left[0.610 \exp \left(\frac{17.27T}{T + 237.3} \right) \right]}{(T + 237.3)^2} \quad (9)$$

where T is the average temperature (°C). In addition, the psychrometric constant can be expressed as follows [72]:

$$\gamma = C_p p / 0.622l \quad (10)$$

where C_p is the specific heat capacity of air at the pressure 1.013×10^{-3} (MJ/kg/°C), l is the latent heat of vaporization, 2.45 (MJ/kg), and p is the atmospheric pressure (kPa), which is a function of the elevation of the location, expressed as follows [73]:

$$p = 1.013 \left(\frac{293 - 0.0065z}{293} \right)^{5.26} \quad (11)$$

where z is the height of the location above the sea level (m). In Equation (8), the linear approximation wind function $f(U_2)$ requires the wind speed at 2 m height. Since most wind speed measurement takes place at 10 m, the linear approximation is expressed as follows [74]:

$$f(U_2) = 0.26(1 + 0.54U_2) \quad (12)$$

where U_2 represents the wind speed at 2 m height (m/s). Its relation to the wind speed at 10 m height is given by the following:

$$U_2 = U_{10} \frac{4.87}{\ln(67.8Z_{10} - 5.42)} \quad (13)$$

where U_{10} is the wind speed measured at 10 m height and Z_{10} is the reference height (10 m). The net radiation (R_n) in Equation (8) is a function of the vapor pressure (e_a) which can be described as follows [70]:

$$R_n = (1 - \alpha)Q_a \left(0.18 + 0.55 \frac{n}{N}\right) - \sigma(T + 273.2)^4 (0.56 - 0.092 \times 0.866\sqrt{e_a}) \left(0.1 + 0.9 \frac{n}{N}\right) \quad (14)$$

where R_n is the net radiation ($\text{MJ}/\text{m}^2/\text{d}$), and α is the albedo, the fraction of solar radiation reflected by the surface. Its value can range between 0.05 and 0.95. Q_a is the extra-terrestrial solar radiation ($\text{MJ}/\text{m}^2/\text{d}$), n is the duration of sunshine for the day (hours), N is the maximum possible duration of sunshine or daylight hours (hours), σ is the Stefan–Boltzmann constant, 4.903×10^{-9} ($\text{MJ}/\text{K}^4/\text{m}^2/\text{d}$), T is the air temperature ($^{\circ}\text{C}$), and e_a is the actual vapor pressure (kPa).

In Equation (14), the duration of sunshine hours (n) can be evaluated by the correlation of precipitation, wind speed, and relative humidity, given by the following [75]:

$$n = 9.679 - 0.001P - 0.542Ws - 0.053RH \quad (15)$$

where P is the precipitation, Ws is the wind speed at 10 m height, and RH is the relative humidity. The maximum possible duration of sunshine or daylight hours (N) in Equation (14) can be described using the following relationship [76]:

$$N = \frac{24}{\pi} \omega_s \quad (16)$$

where ω_s is the sunset hour angle (rad) given by the following [76]:

$$\omega_s = \arccos(-\tan\phi \tan\delta) \quad (17)$$

where ϕ is the latitude of the location (rad) and δ is the solar declination evaluated by the following [76]:

$$\delta = 0.409 \sin\left(\frac{2\pi}{365}J - 1.39\right) \quad (18)$$

where δ is the solar declination (rad) and J is the number of days in the year with values between 1 and 365. The actual vapor pressure (e_a) in Equations (8) and (14) can be evaluated as follows [71]:

$$e_a = 0.6108 \exp\left[\frac{17.27T_{dew}}{T_{dew} + 237.3}\right] \quad (19)$$

where T_{dew} is the dew point temperature ($^{\circ}\text{C}$). The advection energy in Equation (8) can be empirically described as follows [70]:

$$M = (0.66B - 0.44R_n) \quad (20)$$

where M is the advection energy ($\text{MJ}/\text{m}^2/\text{d}$), and R_n is the net radiation. The parameter B denotes the effective long-wave radiation that will occur if the surface temperature equals the air temperature, which can be estimated as follows [70]:

$$B = \varepsilon\sigma(T + 273.2)^4 \left[1 - p_n \left(0.707 + \frac{e_a}{158}\right)\right] \quad (21)$$

$$p_n = 1 + [0.25 - 0.005(e_s - e_a)] \left(\frac{C}{10}\right)^2 \quad (22)$$

where ε is the emissivity of the surface, σ is the Stefan–Boltzmann constant, T is the air temperature ($^{\circ}\text{C}$), and e_a remains as described above, while e_s is the saturated vapor pressure (kPa) and C is the cloud amount. The saturated vapor pressure is estimated by the following [71]:

$$e_s = 0.6108 \exp\left[\frac{17.27T}{T + 237.3}\right] \quad (23)$$

where T is the air temperature ($^{\circ}\text{C}$). The cloud amount in Equation (22) can be estimated from the sunshine and daylight hours given by the following [77]:

$$C = (1 - n/N) \quad (24)$$

where C is the cloud amount (okta), and n and N remain as previously defined.

2.3. Estimation of the Base Flow

In this study, we lump the ground water flow and base flow together as base flow. As illustrated in Figure 2, the total flow to the river comprises the quick (or direct) and the base flow. Quick flow is due to rainfall events and typically drops to 0 between such events. Base flow is a continuous long-term flow [78]. Therefore, we have the following:

$$Q_t = Q^{RS} + Q^{baseflow} \quad (25)$$

where Q_t is the total discharge and $Q^{baseflow}$ is the base flow.

The base flow comes from shallow and deep subsurface flow and is an important part of a groundwater system [79]. During the dry season, the river flow is composed mainly of base flow. In wet seasons, river discharge comprises base flow and quick flow [80]. Unfortunately, base flow is difficult to measure by direct methods and is commonly estimated using different approaches [81], e.g., linear reservoir [82], exponential recession [83], UKIH technique [79], recursive digital filtering [84], the pilot point method [81], and the constant, monthly-varying method [85]. Since base flow is relatively stable with slight variations between rainfall events [84,86], we use the monthly-varying method to estimate it in this study. This method assumes a constant base flow for each month of the year, depending on the monthly precipitation and land use. The base flow for a typical month can be predicted using the following relationship [87]:

$$Q_i^{baseflow} = Precipitation_i * \sum_j C_j A_j \quad (26)$$

where $Q_i^{baseflow}$ is the baseflow in month i and $Precipitation_i$ is the total precipitation that occurred in month i . In addition, j is the index of land use activity, which can be residential, agriculture, forest, pasture, wetland, or water bodies. C_j refers to the respective land use coefficients, while A_j represents the respective area covered by land use.

After calculating the total discharge in Equation (25), the river flow can be described as an open channel with uniform flow and, for the properties of the channel, we assume that the cross-section, flow rate, area of flow, depth of flow, and the flow velocity do not change along the channel segment. In addition, the channel where the hydrokinetic turbine will be installed is assumed to have a rectangular shape, as seen in Figure 2. Finally, the velocity of the channel can be obtained as follows:

$$V_{ch} = Q_t / A_{ch} \quad (27)$$

where V_{ch} is the flow velocity (m/s), Q_t is the total discharge (m^3/s), and A_{ch} is the cross-sectional area of the channel (m^2). The cross-sectional area of the channel is expressed as follows:

$$A_{ch} = B_w * y \quad (28)$$

where B_w is the width of the channel (m) and y is the channel depth (m) (see Figure 2).

3. System Modeling of the Proposed HRES

Figure 3 depicts a HRES considered in this study when incorporating the hydrokinetic turbine (HKT). The PV panel and battery storage are connected to the DC bus, whereas the diesel generator, HKT, wind turbine, and the electric load are connected to the AC bus. In between is the bidirectional converter that converts current from DC to AC and vice versa.

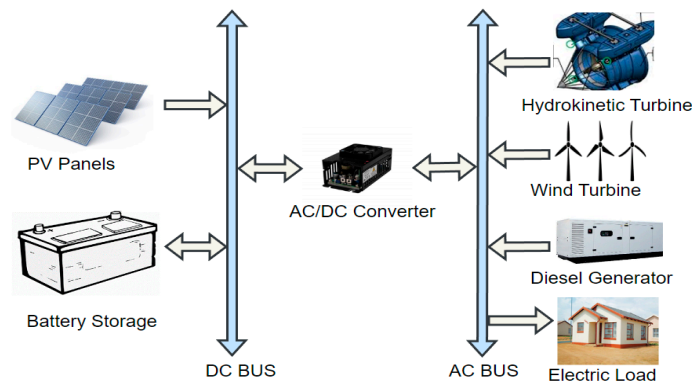


Figure 3. Schematic depiction of a HRES.

3.1. PV Model

The amount of power generated by the PV panels depends on the size of the panels, the solar irradiance, and the ambient temperature. The PV output power for each panel is given as follows [88]:

$$P_{pv}(t) = f_{pv} \left(\frac{G_i(t)}{G_{STC}} \right) [1 + \lambda_p (T_c(t) - T_{c,STC})] \tag{29}$$

where P_{pv} is the panel output power (kW), f_{pv} is the derating factor (%), G_i is the solar irradiance (kW/m^2), G_{STC} is the solar irradiance level at the standard test condition (STC) with a value of $1 \text{ kW}/\text{m}^2$, λ_p is the temperature coefficient ($\%/^{\circ}\text{C}$), T_c is the cell operating temperature ($^{\circ}\text{C}$), and $T_{c,STC}$ is the cell temperature measured at STC with 25°C . Moreover, the cell temperature T_c is expressed as follows [88]:

$$T_c(t) = T_a(t) + G_i(t) \left(\frac{T_{c,NOCT} - T_{a,NOCT}}{G_{NOCT}} \right) * \left(1 - \frac{n_{pv}}{\tau\alpha} \right) \tag{30}$$

where T_a is the ambient temperature ($^{\circ}\text{C}$), $T_{c,NOCT}$ is the nominal operating cell temperature ($^{\circ}\text{C}$), $T_{a,NOCT}$ is the ambient temperature at which the NOCT condition is defined (20°C), G_{NOCT} is the solar irradiance defined for NOCT as $0.8 \text{ kW}/\text{m}^2$, n_{pv} is the PV conversion efficiency (%), and $\tau\alpha$ is the effective solar transmittance–absorptance of the PV with an assumed value of 0.9.

In addition, the total power generated by the PV with multiple panels can be expressed as follows:

$$P_{P_{pvT}}(t) = S_{pv} * P_{pv} \tag{31}$$

where S_{pv} is the size or rated capacity of the PV panel.

3.2. Wind Power Model

The wind power output of a wind turbine is dependent upon the wind speed described as follows [89]:

$$P_w(v(t)) = \begin{cases} 0, & v \leq V^{in} \\ \frac{1}{2} C_p \rho A_{wt} v(t)^3, & V^{in} < v < V^{rate} \\ P^{rate}, & V^{rate} \leq v \leq V^{out} \\ 0, & v \geq V^{out} \end{cases} \tag{32}$$

where $P_w(v(t))$ is the output power of the wind turbine at a wind speed of v (m/s) for a given time (t). A_{wt} is the swept area of the wind turbine (m^2), V^{in} is the cut-in speed, (m/s), V^{out} is the cut-out speed (m/s), C_p is the power coefficient of performance, P^{rate} is the rated power of the wind turbine (kW) at a rated speed of V^{rate} (m/s), while ρ is the air density (kg/m^3). The total power generated by multiple wind turbines will be as follows:

$$P_{W,T}(t) = N_w * P_w(v(t)) \quad (33)$$

where N_w is the number of wind turbines.

3.3. Hydrokinetic Model

The hydrokinetic power (HKP) obtainable from a river channel is a function of the density of water, the cross-sectional area, and the water velocity. Similar to the wind model, the power output of a hydrokinetic turbine can be calculated by the following [54]:

$$P_{HKT}(v_w(t)) = \begin{cases} 0, & v_w \leq v_w^{in} \\ \frac{1}{2} C_{p,H} \rho_w \eta_{HKT} A_{HKT} v_w(t)^3, & v_w^{in} < v_w < v_w^{rate} \\ P_{HKT}^{rate}, & v_w \geq v_w^{rate} \\ 0, & v_w \geq v_w^{out} \end{cases} \quad (34)$$

where $P_{HKT}(v_w(t))$ is the power of a HKT (kW), v_w is the water flow velocity (m/s) at a given time (see Equation (27)), A_{HKT} is the swept area of the rotor blades (m^2), ρ_w is the density of water (kg/m^3), η_{HKT} is the combined HKT-generator efficiency, $C_{p,H}$ is the HKT power coefficient, v_w^{in} is the cut-in water velocity, v_w^{out} is the cut-out water velocity, v_w^{rate} is the rated water velocity, and P_{HKT}^{rate} is the rated power of HKT.

To increase the output capacity of hydrokinetic energy, an array of turbines can be used, and the total power output will be as follows:

$$P_{HKT,T}(t) = N_{HKT} * P_{HKT}(v_w(t)) \quad (35)$$

where N_{HKT} is the number of hydrokinetic turbines.

3.4. Battery Storage Model

Batteries are operated in charging and discharging modes. When there is surplus of energy from the PV, wind and hydrokinetic sources, the battery operates in the charging mode, and its capacity is expressed as follows [6]:

$$C_B(t) = C_B(t-1) * (1 - \sigma) + \left(P_{g,res}(t) - \frac{P_l(t)}{\eta_{con}} \right) * \eta_{bc} \quad (36)$$

When the generated renewable energy is not sufficient to supply the demand, a deficit occurs, and the battery is expected to operate in the discharging mode to cover the deficit. During discharging, the capacity is calculated as follows [6]:

$$C_B(t) = C_B(t-1) * (1 - \sigma) - \left(\frac{P_l(t)}{\eta_{con}} - P_{g,res}(t) \right) / \eta_{bd} \quad (37)$$

In Equations (36) and (37), $P_{g,res}$ is the total generated renewable energy, given as follows:

$$P_{g,res}(t) = P_{P_{pvT}}(t) + P_{W,T}(t) + P_{HKT,T}(t) \quad (38)$$

In Equations (36) and (37), $C_B(t)$ is the available energy of the battery at the current time and $C_B(t-1)$ is that at the last time point. Furthermore, σ is the self-discharge rate of the battery, P_l is the AC load demand of the system, η_{con} is the converter efficiency, η_{bc} is the battery charge efficiency, and η_{bd} describes the battery discharge efficiency. Moreover, the battery should be constrained as follows:

$$C_{Bmin} \leq C_B(t) \leq C_{Bmax} \quad (39)$$

where C_{Bmin} is the minimum energy limit which can be calculated by the following:

$$C_{Bmin} = (1 - DOD) * C_{Bat} \quad (40)$$

where DOD is the depth of discharge and C_{Bat} is the nominal capacity of the battery (Ah). The maximum energy limit C_{Bmax} can be taken as C_{Batt} [48].

Batteries are connected in series, parallel, or a combination to form a battery bank. The total capacity of the battery bank can be represented by the number of batteries and the nominal capacity of each battery, expressed as follows [49]:

$$C_{Bat,T} = N_{Bat} * C_{Bat} \quad (41)$$

where $C_{Bat,T}$ is the total capacity, N_{Bat} is the number of batteries, and C_{Bat} is the nominal capacity of each battery.

3.5. Diesel Generator Model

A diesel generator is used to supply the load when both the renewable energy sources and battery bank fail to satisfy the demand. Its fuel consumption is calculated as follows [90]:

$$f_{cons}(t) = \varphi P_{DG,disp}(t) + \beta P_{rated} \quad (42)$$

where f_{cons} is the fuel consumption of the diesel generator (l/h), $P_{DG,disp}$ is the dispatched power by DG (kW), P_{rated} is the rated capacity, and φ and β are the coefficients of the fuel consumption curve (L/kW/h), with typical values of 0.0140 and 0.244, respectively. The dispatchable power of a diesel generator should operate within a specified range, as follows [91]:

$$P_{DG}(t) = \begin{cases} 0.3P_{rated} \leq P_{DG,disp}(t) \leq P_{rated} \\ 0, & otherwise \end{cases} \quad (43)$$

3.6. Power Converter Model

The rated power of a converter depends on the peak load. The converter efficiency is calculated as follows [6]:

$$\eta_{con} = \frac{P_{output}}{P_{input}} \quad (44)$$

where P_{output} and P_{input} describe the output and input power flows from/to the power converter, respectively.

4. Problem Formulation and Solution Approach

In this study, we evaluate the system performance by the total net present cost (TNPC), since it contains all the associated costs through the project's lifespan. These costs include initial capital, replacement, operation and maintenance, and fuel costs. Thus, TNPC is defined as the objective function to be minimized for an optimal solution. The decision variables are size of PV panels (S_{PV}), the number of wind turbines (N_w), the number of hydrokinetic turbines (N_{HKT}), number of batteries (N_{bat}), and the size or rated power of the diesel generator (S_{DG}). The optimization problem is formulated as follows:

$$\min TNPC(S_{PV}, N_w, N_{HKT}, N_{bat}, S_{DG}) \quad (45)$$

s.t

$$S_{PV,min} \leq S_{PV} \leq S_{PV,max} \quad (46)$$

$$N_{w,min} \leq N_w \leq N_{w,max} \quad (47)$$

$$N_{HKT,min} \leq N_{HKT} \leq N_{HKT,max} \quad (48)$$

$$N_{bat,min} \leq N_{bat} \leq N_{bat,max} \quad (49)$$

$$S_{DG,min} \leq S_{DG} \leq S_{DG,max} \quad (50)$$

$$LSPS_{min} \leq LSPS \leq LSPS_{max} \quad (51)$$

The expressions in Equations (46)–(51) are the constraints of the optimization problem. The last constraint is a reliability indicator referred to as the loss of power supply (*LSPS*) and defined as the ratio of energy deficit to the overall demand of the system [92], as follows:

$$LSPS(\%) = \frac{\sum_{t=1}^{Proj} P_l(t) - P_{pv}(t) - P_w(t) - P_{HKT}(t) - P_{DG}(t) - (C_B(t) - C_{Bmin})}{\sum_{t=1}^{Proj} P_l(t)} \quad (52)$$

where *Proj* stands for the project lifetime (25 years in this study) while all parameters remain as previously defined.

The objective function TNPC in Equation (45) is defined as follows [93]:

$$TNPC = CC + RC + OMC + FC \quad (53)$$

where *CC*, *RC*, *OMC*, and *FC* represent the capital, replacement, operation and maintenance, and total fuel costs of all components associated with the project, respectively. The capital cost of the hybrid energy system can be expressed as follows:

$$CC = C_{cap}^{PV} S_{PV} + C_{cap}^{WT} N_w + C_{cap}^{HKT} N_{HKT} + C_{cap}^{con} S_{con} + C_{cap}^{Bat} N_{Bat} + C_{cap}^{DG} S_{DG} \quad (54)$$

where C_{cap}^{PV} , C_{cap}^{WT} , C_{cap}^{HKT} , C_{cap}^{con} , C_{cap}^{Bat} , and C_{cap}^{DG} are the respective costs of the PV (per kW), wind turbine (per unit), hydrokinetic turbine (per unit), converter (per KW), battery storage (per unit), and DG (per KW). S_{PV} , N_w , N_{HKT} , S_{con} , N_{bat} , and S_{DG} denote the size or rated capacity of PV, the number of wind turbines, the number of hydrokinetic turbines, the size of the converter, the number of batteries, and the size of the DG, respectively.

In Equation (53), the replacement cost can be expressed as follows [6]:

$$RC = C_{rep}^{PV} \cdot S_{PV} \cdot \sum_{k=25}^{Proj} \frac{1}{(1+i)^k} + C_{rep}^{WT} \cdot N_w \cdot \sum_{k=20}^{Proj} \frac{1}{(1+i)^k} + C_{rep}^{HKT} \cdot N_{HKT} \cdot \sum_{k=20}^{Proj} \frac{1}{(1+i)^k} + C_{rep}^{con} \cdot S_{con} \cdot \sum_{k=10,20}^{Proj} \frac{1}{(1+i)^k} + C_{rep}^{Bat} \cdot N_{bat} \cdot \sum_{k=5,10,15,20}^{Proj} \frac{1}{(1+i)^k} + C_{rep}^{DG} \cdot S_{DG} \cdot \sum_{k=a,2a,\dots,<Proj}^{Proj} \frac{1}{(1+i)^k} \quad (55)$$

where C_{rep}^{PV} , C_{rep}^{WT} , C_{rep}^{HKT} , C_{rep}^{con} , C_{rep}^{Bat} , and C_{rep}^{DG} are the respective replacement costs of the PV, wind turbine, hydrokinetic turbine, power converter, batteries, and diesel generator. k represents the specific year in which the particular component will be replaced (e.g., the battery will be replaced every 5 years). In the case of the diesel generator, the lifespan is evaluated based on the operational hours. When the running hours of the DG are equivalent to the manufacturer specified operating hours, then the DG needs replacement. The expression $\frac{1}{(1+i)^k}$ in Equation (55) represents the discount factor (a ratio that describes the present value of a cash flow that occurs in any year of the project lifespan), while i is the real interest rate.

In Equation (53), the operation and maintenance cost can be evaluated as a percentage of the capital cost given by the following [6]:

$$OMC(\$) = \left(\sum_j P_j C_{cap_j} NS_j + f * Oper_{hours} \right) \left[\sum_{k=1}^{Proj} \frac{1}{(1+i)^k} \right] \quad (56)$$

where j is the index of the respective component (PV, WT, HKT, battery, converter), P_j are the corresponding percentages of the capital cost of the respective component, C_{cap_j} is the capital cost of the respective component, and NS_j is the number or size of the respective component (e.g., size for PV and number for HKT). Regarding the diesel generator, the

operation and maintenance cost is evaluated based on the annual operation hours. Hence, f is the hourly operational and maintenance cost, and $Oper_hours$ describes the total diesel generator running hours in a year. The total fuel cost in Equation (53) is calculated by the following [6]:

$$FC(\$) = C_{fuel}^{DG} \cdot f_{cons} \cdot \sum_{k=1}^{Proj} \frac{1}{(1+i)^k} \quad (57)$$

where C_{fuel}^{DG} and f_{cons} are, respectively, the fuel cost and the fuel consumed during the operation of the DG.

Another important performance criterion for evaluating a HRES is the cost of energy (COE). COE describes the system costs over the useful energy provided by the system during the stipulated time period, as follows [92]:

$$COE = \frac{C_{ann}}{total\ load\ served} \quad (58)$$

where C_{ann} is the annualized cost of the system, defined as follows [6]:

$$C_{ann}(\$) = TNPC * CRF \quad (59)$$

where CRF is the capital recovery factor which is defined as a function of the real interest rate i and the useful lifetime of the project [94].

$$CRF(i, Proj) = \frac{i(1+i)^{Proj}}{(1+i)^{Proj} - 1} \quad (60)$$

The optimization problem formulated above leads to a combinatorial nonlinear optimization problem. We use a genetic algorithm (GA) to solve this problem. The GA is widely used in solving complicated combinatorial optimization problems in the energy field. The GA follows the principle of natural selection that mimics biological evolution. Rather than the traditional optimization approach in which a single solution is generated, a GA generates multiple candidate solutions using techniques inspired by natural evolution, such as inheritance, mutation, selection, and crossover [95]. When a configuration fails to satisfy the constraints, it is replaced by a better one during the optimization process. The GA searches for the optimal solution that minimizes the objective function and satisfies the constraints. After the selection process, the solution will then be subject to crossover and mutation operations to produce the next population until a pre-specified number of generations is reached/or when a criterion that determines the convergence is satisfied.

Various studies have applied a genetic algorithm [93,96–98] in the optimal design and operation of hybrid energy systems. The GA has no restrictions regarding the model of the system or the type of decision variables (discrete, continuous, or mixed) [96]; hence, these features make the employment of the GA suitable for our purpose. In this study, the numerical implementation of solving the optimization problem and associated constraints is performed using the GA tool in the MATLAB environment. For solving the case study problems presented in the next section, Table 2 shows the minimum and maximum bounds of the decision variables and constraints, while Table 3 shows the parameters of the GA.

Table 2. Optimization parameters and constraints used in the case study.

Parameter	S_{PV} (kW)	N_w (Unit)	N_{HKT} (Unit)	N_{Bat} (Unit)	S_{DG} (kW)	$LSPS(\%)$
Lower bound	0	0	0	0	80	0
Upper bound	500	10	5	300	300	2

Table 3. GA parameters used in the case study.

Parameter	Value
Population size	50
Maximum number of iterations	500
Crossover fraction	0.8
Function tolerance	1e-6
Constraint tolerance	1e-3
Selection function	Stochastic uniform

5. A Case Study

An off-grid area in Nigeria is selected for a case study to verify our approach. Koluama is a remote community located in Nigeria's coastal Niger Delta region. The community has a nearby river network. The location has an altitude of 6.1 m and a corresponding latitude and longitude of 4°47' N and 5°77' E, respectively [99]. The mean annual rainfall ranges between 2000 and 4000 mm [100]. As is typical in the Niger Delta region, the area is dominated by tropical rainforests, mangrove swamps, mangrove forests, and salt- as well as freshwater zones. The average annual temperature varies between 25 and 32 °C [101].

One of the community's significant challenges, apart from a non-accessible road network, is the lack of an electricity supply. Extending the grid line to such riverine areas will require political 'will' and high investment costs. Though the community has the potential to harness renewable energy resources, a diesel generator is used to meet the load demand. Moreover, high fuel consumption, high maintenance cost, and high emission of greenhouse gases and other pollutants are some setbacks associated with running diesel generators continuously [102]. These setbacks lead to the motivation to utilize the locally available renewable energy resources to complement the diesel generator for energy supply.

5.1. Data Acquisition for Estimating the Flow Velocity

The meteorological data for the studied area required for running the water cycle model is obtained from the NASA Prediction of Worldwide Energy Resources website [103]. A 10-year dataset covering the period of January 2011–December 2021 was used for the study. The dataset comprises precipitation, solar radiation, wind speed, daily temperature, relative humidity, and dew point temperature. These datasets are used to evaluate the abstraction, evapotranspiration, and base flow components. The daily sunshine hours, daylight hours, and cloud amounts are calculated based on the equations shown in Section 2.

To ascertain a coverage area and obtain the soil data (cover/type) and land use, a digital elevation model (DEM) for the Koluama location, i.e., an image in a 30 m × 30 m resolution, is obtained from the Shuttle Radar Topography Mission (SRTM), as seen in Figure 4 [104]. The total area considered within the location is approximately 184 km². Using the DEM, soil data is obtained from the digital soil map of the world [105]. Further descriptions of the datasets used with their corresponding sources are tabulated in Table 4. The composition of the soil data, as seen from the soil map in Figure 4 and Table 5, shows that the study area comprises clayey soil, loamy soil, and water bodies.

Table 4. Topographical and meteorological data of the study area.

Data Type	Description	Resolution	Remark	Source
Topography map	Digital elevation model (DEM)	30 m × 30 m	Shuttle Radar Topography Mission	SRTM [104]
Land use map	Land use	30 m	Landsat Mission	Landsat 7 [106]
Soil map	Soil type and texture	10 km	Digital Soil Map of the World	DSMW [105]
Weather data	Solar radiation, wind speed, precipitation, etc.		Prediction of Worldwide Energy Resources	NASA [103]

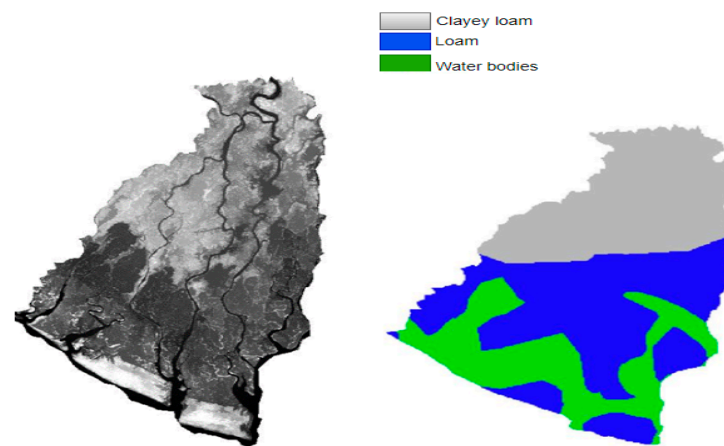


Figure 4. Digital elevation model (left) and soil type/cover (right) of the study area.

Table 5. Data on soil composition.

S/N	Description	Area (km ²)	% of the Area
1	Clayey loam	45.32	24.52
2	Loam	89.76	48.57
3	Water bodies	49.72	26.91

In addition, to obtain the land use data, the land use map of the study area is extracted through a satellite Landsat image with a 30 m resolution [106]. The land classification is based on the supervised maximum likelihood method to determine the land use activities. This process is performed on the ArcGIS (geographic information system software) platform. Table 6 shows that the land use is dominated by swamps and forests, with little residential use. Both the soil and land use data are used to calculate the CN number.

Table 6. Data on land use.

S/N	Description	Area (km ²)	% of the Area
1	Barren land	10.26	5.58
2	Residential	2.28	1.24
3	Forest, woods, and swamps	56.08	30.48
4	Pasture	30.69	16.68
5	Agricultural	41.62	22.62
6	Bare soil	27.85	15.14
7	Water	15.19	8.26

The geometry of the water channel (width (B_w) and depth (y)) is needed to calculate the cross-sectional area (A_{ch}) for hydrokinetic power harnessing. Since we do not have the actual measured dimensions of the channel, reference is made to existing HKTs with their respective rotor diameter. In [107], the Garman Thropton river turbine has a diameter of 1.8 m and requires a depth of at least 1.75 m for turbine installation. Similarly, ref. [51] utilized the river turbine manufactured by Smart Hydropower. The turbine has a rotor diameter of 1 m. The dimension of the channel in which the turbine was utilized prior to enhancement is 1.5 m in depth and 4.8 m in width. It follows that the depth of the channel should be at least equal to or greater than the rotor diameter of the turbine. Furthermore, the area of the channel should be able to cover the swept area of the rotor diameter. In our case study, we selected a 27 kW hydrokinetic turbine with a rotor diameter of 3 m (see Section 5.4). Since the turbine is an underwater turbine that will be submerged, we selected a channel geometry that can accommodate it in case of installation. Therefore, our assumed dimensions for the channel are 6 m in depth and 4 m in width.

5.2. Meteorological Data for HRES

The meteorological data used for the HRES are also accessed from the NASA Prediction of Worldwide Energy Resources website [103]. Table 7 shows the monthly average solar radiation, wind speed, and temperature values in the studied area. The data indicates moderate solar radiation in the range of 3.64 in July to 5.91 kWh/m²/d in February, with an annual average of 4.70 kWh/m²/d. As expected, there is a daily variation of solar radiation for different days and seasons of the year. Radiation values for a typical day in January are usually higher than in July due to the seasonal variations.

Table 7. Solar radiation, wind speed, and temperature of the area.

Month	Jan.	Feb.	March	April	May	June	July	Aug.	Sept.	Oct.	Nov.	Dec.
Solar radiation (kWh/m ² /d)	5.79	5.91	5.49	5.29	4.60	3.67	3.64	4.33	4.30	4.76	5.40	5.60
Wind speed (m/s)	3.35	3.65	3.94	3.92	2.83	4.56	5.27	5.38	4.89	4.11	2.97	3.00
Temperature (°C)	26.17	27.07	27.32	27.16	26.78	25.88	25.10	24.85	25.09	25.59	26.23	26.30

The wind speed varies between 2.83 m/s in May and 5.27 m/s in July. Moreover, a reasonably high wind speed occurs in August and September. On a typical day, the wind speed can reach a lower value of 0.5 m/s in May and a higher value of 8.7 m/s in August. The annual average is 3.66 m/s, as seen in Figure 5a,b.

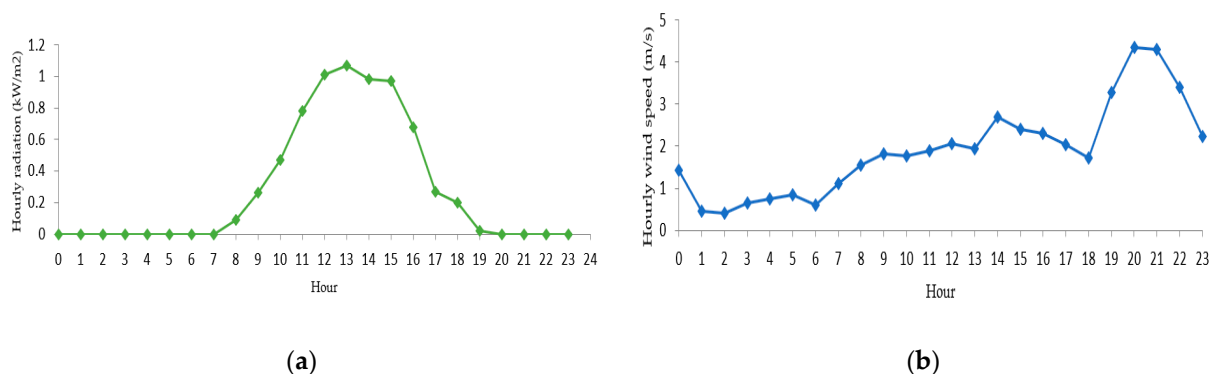


Figure 5. (a) Solar radiation variation for a typical day; (b) hourly wind speed variation.

5.3. Load Demand

Based on the survey and dialog with the end-users, the daily consumption data is generated, and the demand profile is obtained. The daily energy consumption of this community is usually for powering TVs, fridges, lighting, fans, cell phone charging, and other low-energy appliances. Figure 6 describes the demand profile of the community. It is shown that, between 6:00 to 18:00, the energy is consumed mainly by the shops, residential households, and other low-energy loads. Residential consumption is minimal during the day, since most people are off for their respective business activities, such as farming and fishing. Between 19:00 and 23:00, the demand is high since most household members are back home and use electricity for various purposes. Towards midnight, the demand gradually drops as some appliances are switched off. The average daily energy demand is estimated at 860.13 kWh/d, with a peak demand of approximately 100 kW.

5.4. Component Specification of the HRES

The cost, capacity, and other technical details of the system components are relevant for implementing the hybrid energy system model. This study considers the Verdant Power 35 kW hydrokinetic turbine for hydrokinetic power generation. The lifetime, the replacement cost, and other specifications of the components are summarized in Table 8.

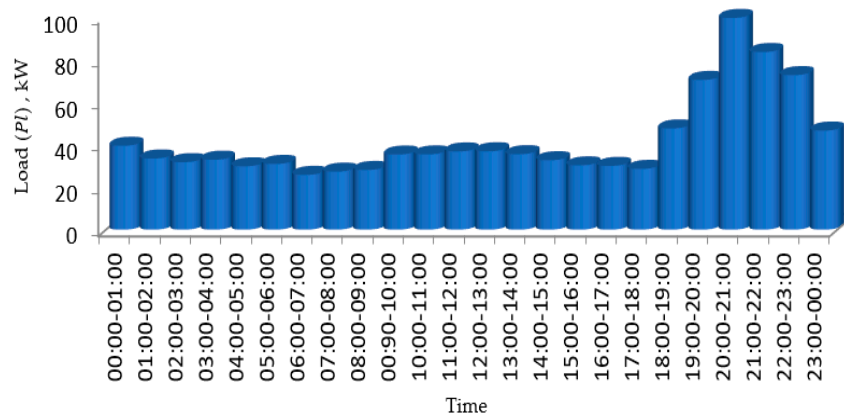


Figure 6. Daily load profile.

Table 8. HRES component specifications.

PV Module	Model: CS6X-325P. Manufacturer: Canadian Solar. Rated capacity: 325 W. Module type: polycrystalline. Efficiency: 16.94%. Temperature power coefficient: $-0.41(\%/^{\circ}\text{C})$. Operating temperature: -40°C to $+85^{\circ}\text{C}$. Lifetime: 25 years [108]. Derating factor: 80%. Capital cost: 664 USD/kW. Replacement cost: 580 USD/kW [109]. Operation and maintenance cost (USD/year): 2% of capital cost.
Wind Turbine	Model: EO25III. Manufacturer: Eocycle. Rated capacity: 25 kW. Cut-in wind speed: 2.75 m/s. Cut-out wind speed: 20 m/s. Rotor diameter: 15.8 m. Lifetime: 20 years [110]. Capital cost: USD 175,000 [111]. Replacement cost: USD 120,000. Operation and maintenance (USD/year): 5% of capital cost.
Hydrokinetic Turbine	Model: TIGRIS-27 H. Rated capacity: 27 kW@2.7 m/s. Cut-in water velocity: 0.5 m/s. Lifetime: 20 years. Number of blades: 3 Rotor diameter: 3 m. Power coefficient: 0.43 [112]. Capital cost: 1150 USD/kW [113]. Replacement: 1000 USD/kW. Operation and maintenance cost (USD/year): 5% of capital cost.
Storage Battery	Model: Surrette 6CS25P. Manufacturer: Rolls. Type: Lead–acid. Nominal voltage: 6V. Nominal capacity: 6.91 kWh. Round trip efficiency: 80%. [114]. Lifetime: 5 years. Capital cost: 271 USD/kWh [115]. Replacement cost: 200 USD/kWh. Operation and maintenance cost (USD/year): 0.5% of the capital cost.
Power converter	Model: S219cph. Manufacturer: Leonics. Rated capacity: 5 kW. DC input voltage: 48 Vdc. Efficiency: 96% [116]. Lifetime: 10 years. Capital cost: 245 USD/kW. Replacement cost: 245 USD/kW [117]. Operation and maintenance cost (USD/year): 4% of capital cost.
Diesel generator	Model: DE150E0. Manufacturer: CAT. Engine speed: 1500 RPM. Lifetime: 60,000 h. Voltage: 400/230 Vac. Frequency: 50 Hz [118]. Fuel price: 0.7 USD/L. Capital cost: 447 USD/kW [119]. Replacement cost: 400 USD/kW. Operation and maintenance cost (USD/h): 0.4.

6. Results and Discussions

This section presents our computation results for the flow velocity and the off-grid HRES for the case study, based on the proposed approach. The computation and implementation of the proposed model were performed on a desktop computer with a 2.9 GHz Intel Core i7 processor with 16 GB RAM in a MATLAB (2021b) environment.

6.1. Results of Flow Velocity

The results of discharge show that the year's maximum, minimum, and mean discharge are 122.90, 0.395, and 14.52 m^3/s , respectively. A breakdown of the monthly discharge, as depicted in Table 9, indicates that the maximum discharge occurs in September, while the minimum is in December. Moreover, the months of May to October have the highest discharge values (greater than 85 m^3/s). This is not surprising because these

months fall under the wet months in Nigeria (the dry season starts around November and runs till April, while the wet season starts around May and runs till October).

Table 9. Calculated monthly river discharge.

Month	Jan.	Feb.	March	April	May	June	July	Aug.	Sept.	Oct.	Nov.	Dec.
Mean discharge (m ³ /s)	1.48	1.07	6.98	2.75	13.82	31.33	17.39	29.15	33.15	26.62	9.05	0.75
Max discharge (m ³ /s)	9.82	10.91	32.18	19.51	96.57	103.4	109.6	85.10	122.9	86.92	30.04	5.33
Min discharge (m ³ /s)	0.58	0.59	2.96	1.25	4.83	10.49	5.95	10.79	11.66	9.44	3.31	0.39

Figure 7a,b illustrates the relationship between the precipitation and discharge in dry and wet months. Figure 7a shows the contribution of base flow to the total discharge in a time interval between January and March, during which, in the time period B (between the 1st and 15th of February), the daily precipitation is between 0.01 and 0.9 mm. Hence, the base flow contribution of 0.59 m³/s is the primary source of discharge to the river channel. In Figure 7b, the discharge to the river comes from both direct and base flows, due to the wet months (1st September to 31st October) with significant rainfall. The precipitation ranges between 0.39 and 73 mm within this period.

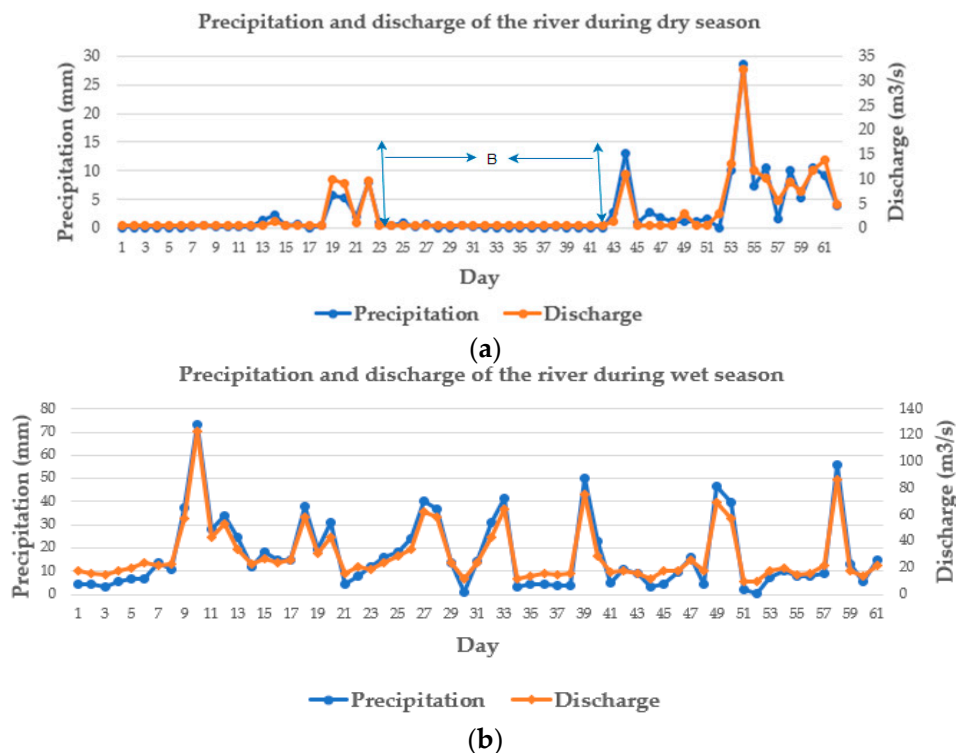


Figure 7. Precipitation and discharge (a) in dry season months and (b) in wet season months.

Our result indicates that the maximum velocity obtained is 5.12 m/s, while the minimum and mean velocities are 0.017 m/s and 0.71 m/s, respectively. Figure 8a,b indicates the daily profile of the flow velocity in both dry (18th February to 31st March) and wet months. It is shown in Figure 8a that the velocity varies between 0.024 and 1.34 m/s. Region C and D are constant velocity periods in which the flow emanates only from the base flow discharge. In region C (22nd–25th February), there is minimal rainfall, and the daily precipitation is less than 1.9 mm. However, the base flow is 0.59 m³/s, resulting in a flow velocity of 0.024 m/s. Similarly, in region D (13th–18th March), the base flow has a constant value of 2.95 m³/s, resulting in a flow velocity of 0.12 m/s.

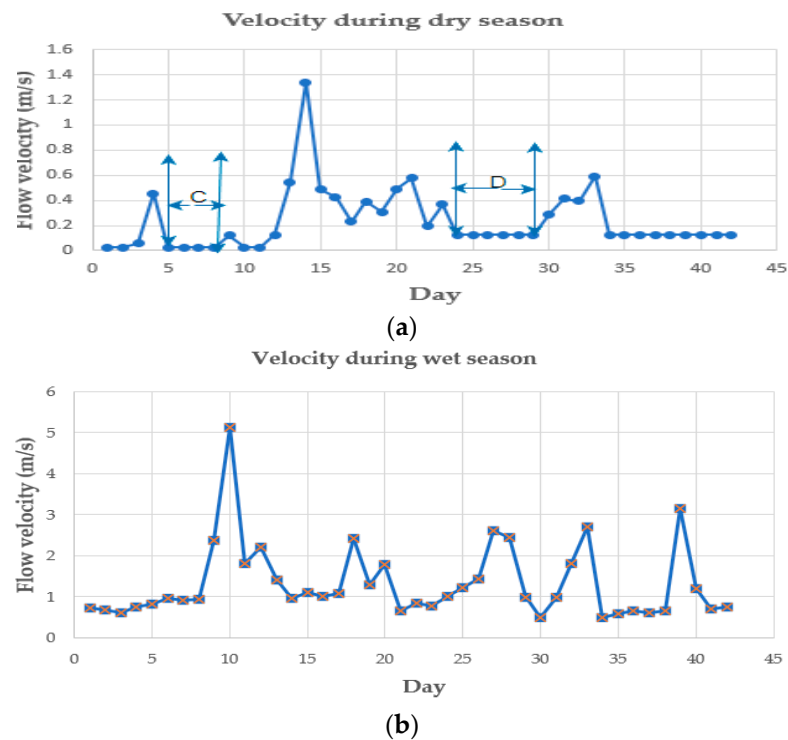


Figure 8. Flow velocity (a) in dry season months and (b) in wet season months.

Figure 8b shows the daily flow velocity of typical wet months (1st September to 12th October). Since there is a significant rainfall, the total discharge comes from both direct and base flows, resulting in the flow velocity ranging between 0.48 and 5.12 m/s. Therefore, the flow velocity is much higher during the wet season due to significant rainfall. Therefore, these months are expected to have the highest hydrokinetic energy contribution to the off-grid HRES.

6.2. Results of the Off-Grid HRES

The HRES architecture is optimized by considering all combinations of the components in the design. The optimal system configuration is found by minimizing the total net present cost and the cost of energy. The decision variables are the sizes of PV panels, the number of WTs, the number of HKTs, the number of batteries, and the size or capacity of the DG. The GA took 204 iterations for the algorithm to reach the optimal solution.

For a lifetime of 25 years and an inflation rate of 11.3%, the resulting optimal architecture consists of 320 kW of PV panels, 120 units of batteries, two hydrokinetic turbines rated 27 kW each, 120 kW converters, zero wind turbines, and a 100 kW diesel generator. With an LSPS of 1.92%, the TNPC and COE are USD 1,103,668 and 0.2841 USD/kWh, respectively. The specified loss of power constraint ($LSPS_{max} = 2$) is satisfied.

6.2.1. Economic Evaluation

The optimal design of the HRES leads to economic parameters, such as capital, replacement, operation and maintenance, and fuel costs of each system component, as shown in Figure 9. It is seen that the total capital cost is USD 573,320, of which 39% is for the battery bank, 37% is for PV panels, 11% is for the HKTs, and 5% is for converters. Furthermore, the battery replacement cost is USD 332,690, the highest among the components. This is not surprising, because the battery lifespan is taken as 5 years; thus, the battery bank needs replacing four times over the total period. Moreover, the contributions of the converter and HKT to the total replacement cost are 7% and 4%, respectively. The PV has no replacement cost, since its lifetime is taken as 25 years. In the same vein, the OM costs for the PV, battery, converter, HKT, and diesel generator are USD 53,607, USD 14,169, USD 14,835, USD 39,168

and USD 711.4, respectively. In addition, the results show that the DG will operate for an average of 141 h yearly, which means the total fuel cost over the project life span is USD 34,822.

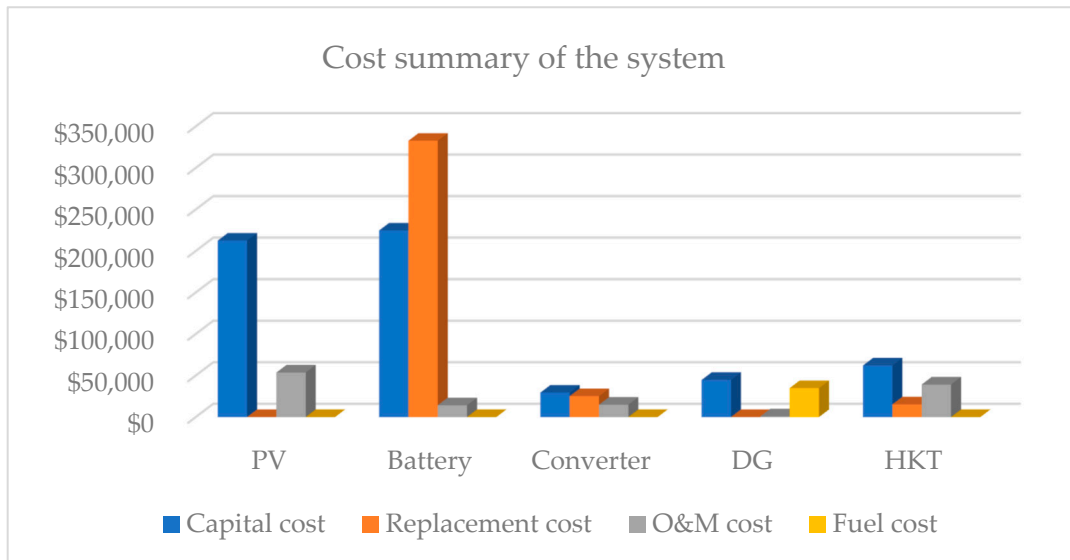


Figure 9. Overall cost summary of the off-grid HRES.

The distribution of costs is shown in Figure 10. It can be seen that the capital cost has the highest proportion, followed by the replacement cost. This is not farfetched because renewable energy technologies are known to have high installation costs.

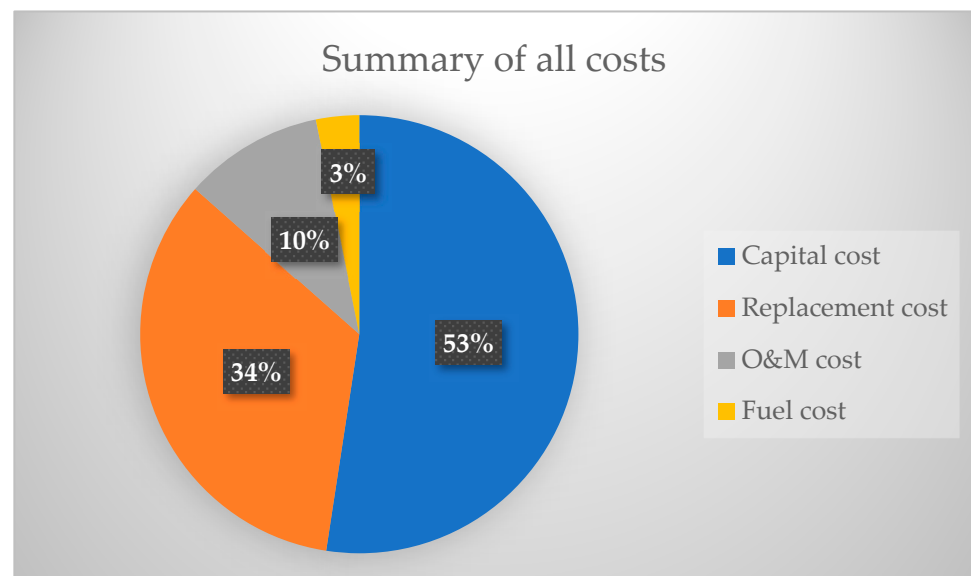


Figure 10. Percentage composition of the various cost of the HRES.

6.2.2. Technical Evaluation

Applying the optimal HRES, the annual load demand of 313,947 kWh/year will be supplied through a combination of PV, hydrokinetic turbine, diesel generator, and battery storage. The total energy generated by the system will be 471, 743 kWh/year. A breakdown of the respective energy sources, as illustrated in Figure 11, shows that the contribution of PV, hydrokinetic turbine, and the diesel generator will be 412,247 kWh/year, 53,852 kWh/year, and 5643 kWh/year, respectively. The total annual load served by the system is 307,940 kWh/year, with a deficit of 6034 kWh/year. It can be observed that

the highest share of energy production is from the PV, followed by the HKT, with DG contributing to only 1% of the total energy.

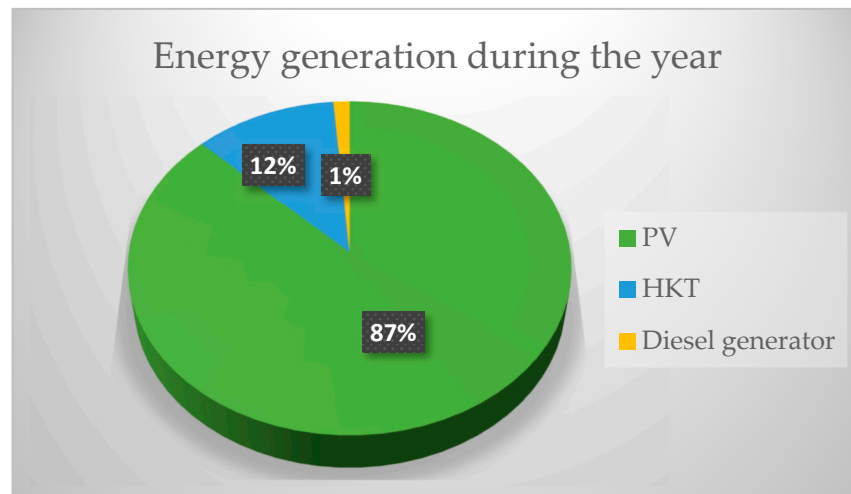


Figure 11. Percentage composition of the yearly energy generation of the HRES.

Further analysis indicates that the maximum output of the PV is 235.4 kW. The energy from PV is mainly generated between 6.00 h and 18.30 h. The output fluctuates within this period, with the peak power mostly occurring at noontime. The maximum power generated by the two units of HKT is 32.4 kW. Since renewable energy sources primarily power the system, the DG operates only 141 h yearly and consumes 3943.5 L of fuel per year with a maximum output of 82.97 kW. Assuming that the yearly running hours of the DG are constant throughout the project lifespan, then the DG will only run 3525 h throughout this period. This is far less than the 60,000 h operational life specified by the manufacturer.

Figure 12 illustrates 3 typical days of hourly generation and dispatch of the battery bank to serve the load demand. At the beginning, the battery bank is assumed to be fully charged with a total maximum capacity of 829.2 kWh. It is seen in Figure 12 that between 1:00 h and 7:00 h, the PV output will be 0 kW due to the unavailability of sunshine. During this period, the power dispatch from the battery and the HKT power will be utilized to supply the load. However, the HKT power is relatively low due to the low flow velocity during this period. The generated power is less than 1 kW, which is insufficient to cover the load demand. Hence, the battery bank will be the major energy source. As can be seen, the battery capacity is reduced from 829.2 kWh to 605.14 kWh within this period.

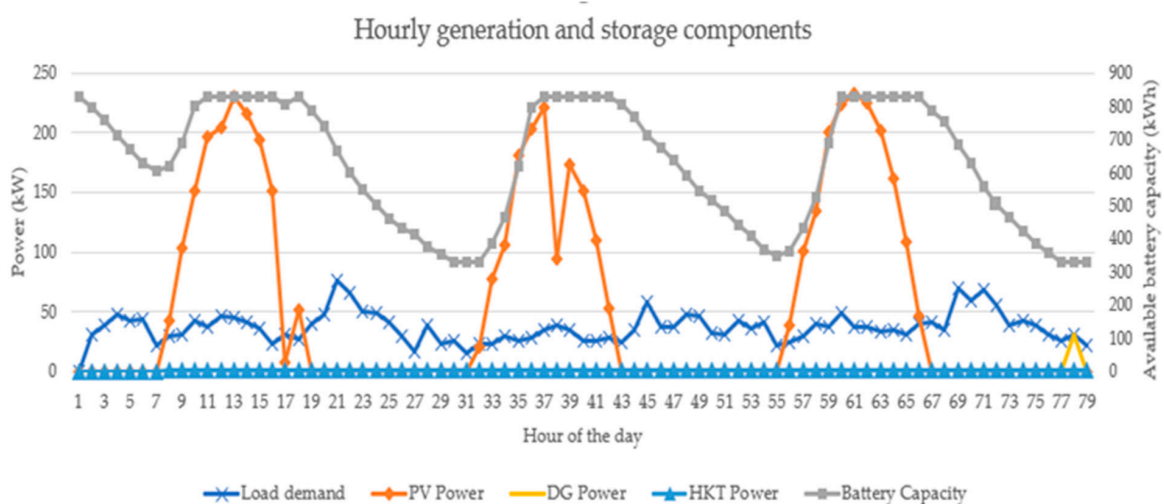


Figure 12. Hourly power profiles.

At 9:00 h, the solar irradiance becomes 0.16 kW/m^2 , and the power output from the PV is increased to 42.56 kW. The total renewable power produced is 42.86 kW, greater than the load demand of 29.51 kW. Thus, the excess energy is charged to the battery bank, then increasing the battery energy to 691.87 kW. There is a load deficit at 76:00 h and 77:00 h because the system fails to satisfy the demand of 25.5 kW and 22 kW, respectively. This is because there is no generation from PV, a minimal generation from HKT, and the battery reaches its minimum energy level (331.68 kWh). Since the load demand in this period is not within the bounds of the DG, there will be no dispatched power from the DG. However, at 78:00 h, the DG will be active and, together with the HKT, will supply the load demand of 31.35 kW.

6.2.3. Comparison with the DG-Only System

Currently, a DG is used as the only source to supply energy to the community. The manufacturer's specification of the DG used in the study indicates that it has an operating life of 60,000 h. However, during the operation, the DG runs for 5925 h instead of 8760 h per year. This is because it assumes that the DG should not be in operation when the load demand is not within its specified bounds. In practice, the DG consumes 166,220 L of fuel annually and generates 243,320 kWh of energy to supply the load demand. However, a total of 25% of the load demand is not met. Table 10 shows that 92% of the cost emanates from the fuel cost, which means that it is expensive for off-grid remote areas to only use diesel generators to satisfy their energy needs. Moreover, the TNPC and COE are USD 1,589,918 and 0.5182 USD/kWh, while the capital, replacement, and OM costs are USD 44,700, USD 47,541 and USD 29,897, respectively.

Table 10. Cost summary of the DG-only system.

Capital Cost (USD)	Replacement Cost (USD)	OM Cost (USD)	Fuel Cost (USD)
44,700	47,541	29,897	1,467,800

For comparison, it can be observed from Table 11 that the capital cost of the optimal HRES is about 11 times of the cost of the DG-only system. However, the operation cost of the DG-only system is exceptionally high compared to the optimal HRES system (USD 1,467,763 compared to USD 34,822). As a result, the TNPC of the DG-only system is about 1.4 times higher than that of the HRES.

Table 11. Comparison of the DG-only and the optimal system.

System	TNPC (USD)	COE (USD/kWh)	Capital Cost (USD)	Fuel Cost (USD)	DG Operation (h/year)	Fuel Consumed (L/year)	Total Load Served (kWh/year)
DG-only	1,589,918	0.5182	44,700	1,467,763	5925	166,220	233,320
Optimal HRES	1,103,668	0.2841	573,320	34,822	141	3943.5	307,940

As shown in Table 11, the DG-only system leads to a COE of 0.5182 USD/kWh compared to 0.2841 USD/kWh obtained by the HRES. It can also be noticed that the DG-only system consumes 166,220 L of fuel annually to serve the load demand during operation. This is 42 times the fuel consumption by the HRES. Moreover, both systems failed to satisfy the annual load demand of 313,947 kWh/year. The annual unmet load of the DG-only system is 80,627 kWh/year, amounting to 25% of the yearly deficit. However, the HRES is able to meet 98.08% of the load demand.

7. Conclusions

Renewable energy sources are clean, efficient, and an excellent alternative to meet the energy demands of off-grid remote areas. To effectively harness the potential of these

resources, it is necessary to embark on technical, economic, and comparative assessment studies to find the most suitable renewable energy resources within a particular location. This paper presents the optimal design of an off-grid hybrid renewable energy that integrates hydrokinetic energy and the commonly used wind, solar, and diesel generators as energy generation sources. A detailed model for estimating the flow velocity of a river is derived based on the water transportation process. This method will benefit off-grid areas where there is no possible measurement of the flow velocity. An optimization problem is formulated and solved to find the optimal configuration and sizing of a HRES. The optimization result for a community in Nigeria shows significant potential for generating hydrokinetic energy, which contributes 38% of the total generation to cover the demand. A summary of the findings of this study are listed below:

- A detailed model of estimating the flow velocity of a river using the water transportation process has been presented in this study. The discharge results show that the maximum, minimum, and mean annual discharge are 122.90, 0.395, and 14.52 m³/s, respectively. Moreover, our result further indicates that the maximum velocity obtained is 5.12 m/s, while the minimum and mean velocities are 0.017 m/s and 0.71 m/s, respectively. This model-based method will benefit off-grid areas that do not have the requisite manpower to obtain measured or observed data.
- The studied community has the potential to harness both solar and hydrokinetic energy. Moreover, wind technology is not an economically viable option compared to others due to the estimated low wind speed obtained in the area and the high cost of the wind generation component.
- The optimization result using GA shows that the optimal system architecture consists of 320 kW of PV panels, 120 units of 6.91 kWh batteries, two (27 kW) hydrokinetic turbines, 120 kW converters, zero wind turbines, and a 100 kW diesel generator. The total net present cost, cost of energy, and capital cost of the system are USD 1,103,668, 0.2841 USD/kWh and USD 573,320, respectively.

In this study, the data and parameters in the model are assumed to be deterministic, particularly in the flow velocity model. Uncertainties, especially the parameters in the flow velocity model, will be considered in our future work to analyze the reliability of the results.

Author Contributions: Conceptualization, G.R.I. and P.L.; methodology, G.R.I.; software, G.R.I.; validation, G.R.I.; formal analysis and investigation, G.R.I.; data curation, G.R.I.; writing—original draft preparation, G.R.I.; writing—review and editing, G.R.I. and P.L.; supervision, P.L.; funding acquisition, G.R.I. All authors have read and agreed to the published version of the manuscript.

Funding: This research was funded by the Deutscher Akademischer Austauschdienst (DAAD) and the Petroleum Technology Development Fund (PTDF) under the Nigerian-German Postgraduate Training Programme with grant number 57401043.

Data Availability Statement: All data sources have been cited within the article.

Conflicts of Interest: The authors declare no conflict of interest.

References

1. IEA. *SDG7: Data and Projections*; IEA: Paris, France, 2019.
2. IEA. *World Energy Outlook 2019*; IEA: Paris, France, 2019.
3. United Nation. Sustainable Development Goals. 2019. Available online: <https://www.un.org/sustainabledevelopment/blog/2019/06/growing-at-a-slower-pace-world-population-is-expected-to-reach-9-7-billion-in-2050-and-could-peak-at-nearly-11-billion-around-2100-un-report/> (accessed on 25 June 2022).
4. Ghiasi, M. Detailed study, multi-objective optimization, and design of an AC-DC smart microgrid with hybrid renewable energy resources. *Energy* **2019**, *169*, 496–507. [CrossRef]
5. Ember; Energiewende, A. Renewable Energies Overtake Gas and Coal in EU Electricity Generation. 2021. Available online: <https://www.agora-energiewende.de/en/press/news-archive/renewables-overtake-gas-and-coal-and-coal-in-eu-electricity-generation-1/#:~:text=For%20the%20first%20time%2C%20more,the%20British%20think%20tank%20Ember> (accessed on 13 June 2022).

6. Mokhtara, C.; Negrou, B.; Bouferrouk, A.; Yao, Y.; Settou, N.; Ramadan, M. Integrated supply–demand energy management for optimal design of off-grid hybrid renewable energy systems for residential electrification in arid climates. *Energy Convers. Manag.* **2020**, *221*, 113192. [[CrossRef](#)]
7. Ighravwe, D.E.; Babatunde, O.M.; Adedoja, O.S.; Okharedia, T.E. Evaluation and selection of hybrid renewable energy systems for healthcare centres in rural areas: A techno-economic approach. In Proceedings of the IEEE International Conference on Adaptive Science and Technology (ICAST), Accra, Ghana, 22–24 August 2018. [[CrossRef](#)]
8. Olatomiwa, L. Optimal configuration assessments of hybrid renewable power supply for rural healthcare facilities. *Energy Rep.* **2016**, *2*, 141–146. [[CrossRef](#)]
9. Babatunde, O.M.; Adedoja, O.S.; Babatunde, D.E.; Denwigwe, I.H. Off-grid hybrid renewable energy system for rural healthcare centers: A case study in Nigeria. *Energy Sci. Eng.* **2019**, *7*, 676–693. [[CrossRef](#)]
10. Ghenai, C.; Bettayeb, M. Modelling and performance analysis of a stand-alone hybrid solar PV/Fuel Cell/Diesel Generator power system for university building. *Energy* **2019**, *171*, 180–189. [[CrossRef](#)]
11. Vishnupriyan, J.; Manoharan, P.S. Optimizing an On-Grid Hybrid Power System in Educational Institution in Tamil Nadu, India. In *Green Buildings and Sustainable Engineering; Proceedings of GBSE 2018*; Springer: Berlin/Heidelberg, Germany, 2019; pp. 93–103.
12. Niemelä, T.; Kosonen, R.; Jokisalo, J. Cost-optimal energy performance renovation measures of educational buildings in cold climate. *Appl. Energy* **2016**, *183*, 1005–1020. [[CrossRef](#)]
13. Soberanis, M.A.E.; Mithruth, T.; Bassam, A.; Mérida, W. A sensitivity analysis to determine technical and economic feasibility of energy storage systems implementation: A flow battery case study. *Renew Energy* **2018**, *115*, 547–557. [[CrossRef](#)]
14. Aderemi, B.A.; Chowdhury, S.P.D.; Olwal, T.O.; Abu-Mahfouz, A.M. Techno-economic feasibility of hybrid solar photovoltaic and battery energy storage power system for a mobile cellular base station in Soshanguve, South Africa. *Energies* **2018**, *11*, 1572. [[CrossRef](#)]
15. Amutha, W.M.; Rajini, V. Techno-economic evaluation of various hybrid power systems for rural telecom. *Renew. Sustain. Energy Rev.* **2015**, *43*, 553–561. [[CrossRef](#)]
16. Baseer, M.A.; Alqahtani, A.; Rehman, S. Techno-economic design and evaluation of hybrid energy systems for residential communities: Case study of Jubail industrial city. *J. Clean Prod.* **2019**, *237*, 117806. [[CrossRef](#)]
17. Hassan, Q. Evaluation and optimization of off-grid and on-grid photovoltaic power system for typical household electrification. *Renew Energy* **2020**, *164*, 375–390. [[CrossRef](#)]
18. Tu, T.; Rajarathnam, G.P.; Vassallo, A.M. Optimization of a stand-alone photovoltaic–wind–diesel–battery system with multi-layered demand scheduling. *Renew Energy* **2019**, *131*, 333–347. [[CrossRef](#)]
19. Veilleux, G.; Potisat, T.; Pezim, D.; Ribback, C.; Ling, J.; Krysztofiński, A.; Ahmed, A.; Papenheim, J.; Pineda, A.M.; Sembian, S.; et al. Techno-economic analysis of microgrid projects for rural electrification: A systematic approach to the redesign of Koh Jik off-grid case study. *Energy Sustain. Dev.* **2020**, *54*, 1–13. [[CrossRef](#)]
20. Johannsen, R.M.; Østergaard, P.A.; Hanlin, R. Hybrid photovoltaic and wind mini-grids in Kenya: Techno-economic assessment and barriers to diffusion. *Energy Sustain. Dev.* **2020**, *54*, 111–126. [[CrossRef](#)]
21. Aziz, A.S.; Tajuddin, M.F.N.; Adzman, M.R.; Azmi, A.; Ramli, M.A.M. Optimization and sensitivity analysis of standalone hybrid energy systems for rural electrification: A case study of Iraq. *Renew Energy* **2019**, *138*, 775–792. [[CrossRef](#)]
22. Shahzad, M.K.; Zahid, A.; Rashid, T.; Rehan, M.A.; Ali, M.; Ahmad, M. Techno-economic feasibility analysis of a solar-biomass off grid system for the electrification of remote rural areas in Pakistan using HOMER software. *Renew Energy* **2017**, *106*, 264–273. [[CrossRef](#)]
23. IEA. *Global Energy Review 2020*; IEA: Paris, France, 2020.
24. IEA. *Renewables 2019*; IEA: Paris, France, 2019.
25. Jacobson, P.T.; Ravens, T.M.; Cunningham, K.W.; Scott, G. *Assessment and Mapping of the Riverine Hydrokinetic Resource in the Continental United States*; EPRI: Palo Alto, CA, USA, 2012. [[CrossRef](#)]
26. Kirke, B. Hydrokinetic turbines for moderate sized rivers. *Energy Sustain. Dev.* **2020**, *58*, 182–195. [[CrossRef](#)] [[PubMed](#)]
27. Olatunji, O.A.S.; Raphael, A.T.; Yomi, I.T. Hydrokinetic energy opportunity for rural electrification in Nigeria. *Int. J. Renew. Energy Dev.* **2018**, *7*, 183–190. [[CrossRef](#)]
28. Chen, Z.; Wang, Z.; Liu, Y.; Wang, S.; Leng, C. Estimating the flow velocity and discharge of ADCP unmeasured area in tidal reach. *Flow Meas. Instrum.* **2016**, *52*, 208–218. [[CrossRef](#)]
29. Cruz, J.d.S.; Blanco, C.J.C.; Junior, A.C.P.B. Flow-velocity model for hydrokinetic energy availability assessment in the amazon. *Acta Sci. Technol.* **2020**, *42*, e45703. [[CrossRef](#)]
30. Khan, M.J.; Iqbal, M.T.; Quaicoe, J.E. River current energy conversion systems: Progress, prospects and challenges. *Renew. Sustain. Energy Rev.* **2008**, *12*, 2177–2193. [[CrossRef](#)]
31. Ibrahim, W.I.; Mohamed, M.R.; Ismail, R.M.T.R.; Leung, P.K.; Xing, W.W.; Shah, A.A. Hydrokinetic energy harnessing technologies: A review Hydrokinetic energy harnessing technologies: A review. *Energy Reports* **2021**, *7*, 2021–2042. [[CrossRef](#)]
32. Arango-manrique, A.; Ricardo, N.; Budes, F.A.B. Energy, Economic, and Environmental Evaluation of a Proposed Solar-Wind Power On-grid System Using HOMER Pro:Case Study in Colombia. *Energies* **2020**, *13*, 16625.

33. Yimen, N.; Hamandjoda, O.; Meva'a, L.; Ndzana, B.; Nghanou, J. Analyzing of a photovoltaic/wind/biogas/pumped-hydro off-grid hybrid system for rural electrification in Sub-Saharan Africa—Case study of Djoundé in Northern Cameroon. *Energies* **2018**, *11*, 2644. [[CrossRef](#)]
34. Oviroh, P.O.; Jen, T.C. The energy cost analysis of hybrid systems and diesel generators in powering selected base transceiver station locations in Nigeria. *Energies* **2018**, *11*, 687. [[CrossRef](#)]
35. Sambhi, S.; Sharma, H.; Bhadoria, V.; Kumar, P.; Chaurasia, R.; Chaurasia, G.S.; Fotis, G.; Vita, V.; Ekonomou, L.; Pavlatos, C.; et al. Economic Feasibility of a Renewable Integrated Hybrid Power Generation System for a Rural Village of Ladakh. *Energies* **2022**, *15*, 9126. [[CrossRef](#)]
36. Cabanero, A.; Nolting, L.; Praktiknjo, A. Mini-grids for the sustainable electrification of rural areas in sub-Saharan Africa: Assessing the potential of keymaker models. *Energies* **2020**, *13*, 6350. [[CrossRef](#)]
37. Islam, M.R.; Akter, H.; Howlader, H.O.R.; Senjyu, T. Optimal Sizing and Techno-Economic Analysis of Grid-Independent Hybrid Energy System for Sustained Rural Electrification in Developing Countries: A Case Study in Bangladesh. *Energies* **2022**, *15*, 6381. [[CrossRef](#)]
38. Costa, T.S.; Villalva, M.G. Technical Evaluation of a PV-Diesel Hybrid System with Energy Storage: Case Study in the Tapajós-Arapiuns Extractive Reserve, Amazon, Brazil. *Energies* **2020**, *13*, 2969. [[CrossRef](#)]
39. Miao, C.; Teng, K.; Wang, Y.; Jiang, L. Technoeconomic analysis on a hybrid power system for the uk household using renewable energy: A case study. *Energies* **2020**, *13*, 3231. [[CrossRef](#)]
40. Gbadamosi, S.L.; Ogunje, F.S.; Wara, S.T.; Nwulu, N.I. Techno-Economic Evaluation of a Hybrid Energy System for an Educational Institution: A Case Study. *Energies* **2022**, *15*, 5606. [[CrossRef](#)]
41. Al-Badi, A.; Al Wahaibi, A.; Ahshan, R.; Malik, A. Techno-Economic Feasibility of a Solar-Wind-Fuel Cell Energy System in Duqm, Oman. *Energies* **2022**, *15*, 5379. [[CrossRef](#)]
42. Amupolo, A.; Nambundunga, S.; Chowdhury, D.S.P.; Grün, G. Techno-Economic Feasibility of Off-Grid Renewable Energy Electrification Schemes: A Case Study of an Informal Settlement in Namibia. *Energies* **2022**, *15*, 4235. [[CrossRef](#)]
43. Sambhi, S.; Sharma, H.; Kumar, P.; Fotis, G.; Vita, V.; Ekonomou, L. Techno-Economic Optimization of an Off-Grid Hybrid Power Generation for SRM IST, Delhi-NCR Campus. *Energies* **2022**, *15*, 7880. [[CrossRef](#)]
44. Samy, M.M.; Barakat, S.; Ramadan, H.S. Techno-economic analysis for rustic electrification in Egypt using multi-source renewable energy based on PV/wind/FC. *Int. J. Hydrogen. Energy* **2020**, *45*, 11471–11483. [[CrossRef](#)]
45. Singh, S.S.; Fernandez, E. Modeling, size optimization and sensitivity analysis of a remote hybrid renewable energy system. *Energy* **2018**, *143*, 719–731. [[CrossRef](#)]
46. Rodriguez-Gallegos, C.D.; Gandhi, O.; Yang, D.; Alvarez-Alvarado, M.S.; Zhang, W.; Reindl, T. A Siting and Sizing Optimization Approach for PV-Battery-Diesel Hybrid Systems. *IEEE Trans. Ind. Appl.* **2018**, *54*, 2637–2645. [[CrossRef](#)]
47. Zhang, W.; Maleki, A.; Rosen, M.A.; Liu, J. Sizing a stand-alone solar-wind-hydrogen energy system using weather forecasting and a hybrid search optimization algorithm. *Energy Convers Manag.* **2019**, *180*, 609–621. [[CrossRef](#)]
48. Fodhil, F.; Hamidat, A.; Nadjemi, O. Potential, optimization and sensitivity analysis of photovoltaic-diesel-battery hybrid energy system for rural electrification in Algeria. *Energy* **2019**, *169*, 613–624. [[CrossRef](#)]
49. Adefarati, T.; Bansal, R.C. Reliability, economic and environmental analysis of a microgrid system in the presence of renewable energy resources. *Appl. Energy* **2019**, *236*, 1089–1114. [[CrossRef](#)]
50. Yuce, M.I.; Muratoglu, A. Hydrokinetic energy conversion systems: A technology status review. *Renew. Sustain. Energy Rev.* **2015**, *43*, 72–82. [[CrossRef](#)]
51. Niebuhr, C.M.; van Dijk, M.; Neary, V.S.; Bhagwan, J.N. A review of hydrokinetic turbines and enhancement techniques for canal installations: Technology, applicability and potential. *Renew. Sustain. Energy Rev.* **2019**, *113*, 109240. [[CrossRef](#)]
52. Abutunis, A.; Taylor, G.; Fal, M.; Chandrashekhara, K. Experimental evaluation of coaxial horizontal axis hydrokinetic composite turbine system. *Renew Energy* **2020**, *157*, 232–245. [[CrossRef](#)]
53. Adeogun, A.G.; Ganiyu, H.O.; Ladokun, L.L.; Ibitoye, B.A. Evaluation of hydrokinetic energy potentials of selected rivers in Kwara state, Nigeria. *Environ. Eng. Res.* **2020**, *25*, 267–273. [[CrossRef](#)]
54. Ladokun, L.L.; Sule, B.F.; Ajao, K.R.; Adeogun, A.G. Resource assessment and feasibility study for the generation of hydrokinetic power in the tailwaters of selected hydropower stations in Nigeria. *Water Sci.* **2018**, *32*, 338–354. [[CrossRef](#)]
55. Eme, L.C.; Ulasi, J.A.; Tunde, A.I.A.; Odunze, A.C. Hydrokinetic turbines for power generation in Nigerian river basins. *Water Pract. Technol.* **2019**, *14*, 71–80. [[CrossRef](#)]
56. John, B.; Thomas, R.N.; Varghese, J. Integration of hydrokinetic turbine-PV-battery standalone system for tropical climate condition. *Renew Energy* **2020**, *149*, 361–373. [[CrossRef](#)]
57. Nag, A.K.; Sarkar, S. Techno-economic analysis of a micro-hydropower plant consists of hydrokinetic turbines arranged in different array formations for rural power supply. *Renew Energy* **2021**, *179*, 475–487. [[CrossRef](#)]
58. Xia, T.; Rezaei, M.; Dampage, U.; Ali Alharbi, S.; Nasif, O.; Borowski, P.F.; Mohamed, M.A. Techno-economic assessment of a grid-independent hybrid power plant for co-supplying a remote micro-community with electricity and hydrogen. *Processes* **2021**, *9*, 1375. [[CrossRef](#)]
59. Islam, M.S.; Das, B.K.; Das, P.; Rahaman, M.H. Techno-economic optimization of a zero emission energy system for a coastal community in Newfoundland, Canada. *Energy* **2021**, *220*, 119709. [[CrossRef](#)]

60. Tigabu, M.T.; Guta, D.D.; Admasu, B.T. Economics of Hydro-Kinetic Turbine for Off-Grid Application: A Case Study of Gumara River, Upper Blue Nile, Amhara, Ethiopia. 2019. Available online: <https://www.researchgate.net/publication/336148737> (accessed on 17 May 2022).
61. Bonakdari, H. Establishment of relationship between mean and maximum velocities in narrow sewers. *J. Environ. Manag.* **2012**, *113*, 474–480. [[CrossRef](#)]
62. Ladokun, L.L.; Ajao, K.R.; Sule, B.F. Hydrokinetic Energy Conversion System Nigeria. *Int. J. Technol.* **2013**, *32*, 538–549.
63. Subramanya, K. *Engineering Hydrology*, 3rd ed.; The McGraw-Hill Companies: New Delhi, India, 2008.
64. Chow, V.T.; Maidment, D.R.; Mays, L.W. *Applied Hydrology*; The McGraw-Hill Companies: New Delhi, India, 1988.
65. Bhatta, B.; Shrestha, S.; Shrestha, P.K.; Talchabhadel, R. Evaluation and application of a SWAT model to assess the climate change impact on the hydrology of the Himalayan River Basin. *Catena* **2019**, *181*, 104082. [[CrossRef](#)]
66. Fan, F.; Deng, Y.; Hu, X.; Weng, Q. Estimating composite curve number using an improved SCS-CN method with remotely sensed variables in guangzhou, China. *Remote Sens* **2013**, *5*, 1425–1438. [[CrossRef](#)]
67. Abdi, I.; Meddi, M. Comparison of conceptual rainfall–runoff models in semi-arid watersheds of eastern Algeria. *J. Flood Risk Manag.* **2021**, *14*, e01620. [[CrossRef](#)]
68. Valiantzas, J.D. Simplified versions for the Penman evaporation equation using routine weather data. *J. Hydrol.* **2006**, *331*, 690–702. [[CrossRef](#)]
69. Khaldi, A.; Khaldi, A.; Hamimed, A. Using the Priestley-Taylor expression for estimating actual évapotranspiration from satellite Landsat ETM + data. *Proc. Int. Assoc. Hydrol. Sci.* **2014**, *364*, 398–403. [[CrossRef](#)]
70. Nakamichi, T.; Moroizumi, T. Applicability of three complementary relationship models for estimating actual evapotranspiration in urban area. *J. Hydrol. Hydromech.* **2015**, *63*, 117–123. [[CrossRef](#)]
71. Singer, M.B.; Asfaw, D.T.; Rosolem, R.; Cuthbert, M.O.; Miralles, D.G.; MacLeod, D.; Quichimbo, E.A.; Michaelides, K. Hourly potential evapotranspiration at 0.1° resolution for the global land surface from 1981-present. *Sci. Data* **2021**, *8*, 224. [[CrossRef](#)]
72. Jabloun, M.; Sahli, A. Evaluation of FAO-56 methodology for estimating reference evapotranspiration using limited climatic data. Application to Tunisia. *Agric. Water Manag.* **2008**, *95*, 707–715. [[CrossRef](#)]
73. Poyen, F.B.; Ghosh, A.K.; Kundu, P.; Sen, K. Sensors & Transducers Analysis of Evaluation Stages Involved in Penman Monteith Equation. 2016. Available online: <http://www.sensorsportal.com> (accessed on 10 April 2022).
74. Hobbins, M.T.; Ramírez, J.A.; Brown, T.C.; Claessens, L.H.J.M. The complementary relationship in estimation of regional evapotranspiration: The Complementary Relationship Areal Evapotranspiration and Advection-Aridity models. *Water Resour. Res.* **2001**, *37*, 1367–1387. [[CrossRef](#)]
75. Yang, Y.H.; Zhao, N.; Hao, X.H.; Li, C.Q. Decreasing trend of sunshine hours and related driving forces in North China. *Theor. Appl. Climatol.* **2009**, *97*, 91–98. [[CrossRef](#)]
76. Dlouhá, D.; Dubovský, V.; Pospíšil, L. Optimal calibration of evaporation models against penman–monteith equation. *Water* **2021**, *13*, 1484. [[CrossRef](#)]
77. Sarkar, M.N.I. Estimation of solar radiation from cloud cover data of Bangladesh. *Renew Wind Water Sol.* **2016**, *3*, 11. [[CrossRef](#)]
78. Duki, S.R.H.; Seyedian, S.M.; Rouhani, H.; Farasati, M.; Professor, A. Evaluation of Base Flow Separation Methods for Determining Water Extraction (Case study: Gorganroud River Basin). *Water Harvest. Res.* **2017**, *2*, 54–70. [[CrossRef](#)]
79. Zhang, J.; Zhang, Y.; Song, J.; Cheng, L. Evaluating relative merits of four baseflow separation methods in Eastern Australia. *J. Hydrol.* **2017**, *549*, 252–263. [[CrossRef](#)]
80. Smakhtin, V.U. Estimating continuous monthly baseflow time series and their possible applications in the context of the ecological reserve. *Water SA* **2001**, *27*, 213–217. [[CrossRef](#)]
81. Capesius, J.P.; Arnold, L.R. Comparison of Two Methods for Estimating Base Flow in Selected Reaches of the South Platte River, Colorado. 2012. Available online: <http://www.usgs.gov/pubprod> (accessed on 20 March 2022).
82. Buytaert, W.; de Bièvre, B.; Wyseure, G.; Deckers, J. The use of the linear reservoir concept to quantify the impact of changes in land use on the hydrology of catchments in the Andes. *Hydrol. Earth Syst. Sci.* **2004**, *8*, 108–114. [[CrossRef](#)]
83. Yang, H.; Choi, H.T.; Lim, H. Applicability assessment of estimation methods for baseflow recession constants in small forest catchments. *Water* **2018**, *10*, 1074. [[CrossRef](#)]
84. Hu, C.; Zhao, D.; Jian, S. Baseflow estimation in typical catchments in the Yellow River Basin, China. *Water Sci. Technol. Water Supply* **2021**, *21*, 648–667. [[CrossRef](#)]
85. Feldman, A. Hydrologic Modeling System HEC-HMS: Technical Reference Manual. US Army Corps of Engineers, Hydrological Engineering Center. 2000. Available online: [https://www.hec.usace.army.mil/software/hec-hms/documentation/HEC-HMS_Technical%20Reference%20Manual_\(CPD-74B\).pdf](https://www.hec.usace.army.mil/software/hec-hms/documentation/HEC-HMS_Technical%20Reference%20Manual_(CPD-74B).pdf) (accessed on 2 July 2022).
86. Piggott, A.R.; Moin, S.; Southam, C. A revised approach to the UKIH method for the calculation of baseflow. *Hydrol. Sci. J.* **2005**, *50*, 911–920. [[CrossRef](#)]
87. Lee, H.; Choi, H.S.; Chae, M.S.; Park, Y.S. A study to suggest monthly baseflow estimation approach for the long-term hydrologic impact analysis models: A case study in south korea. *Water* **2021**, *13*, 2043. [[CrossRef](#)]
88. Mandal, S.; Das, B.K.; Hoque, N. Optimum sizing of a stand-alone hybrid energy system for rural electrification in Bangladesh. *J. Clean Prod.* **2018**, *200*, 12–27. [[CrossRef](#)]

89. Sgobba, A.; Meskell, C. On-site renewable electricity production and self consumption for manufacturing industry in Ireland: Sensitivity to techno-economic conditions. *J. Clean Prod.* **2019**, *207*, 894–907. [CrossRef]
90. Elkadeem, M.R.; Wang, S.; Sharshir, S.W.; Atia, E.G. Feasibility analysis and techno-economic design of grid-isolated hybrid renewable energy system for electrification of agriculture and irrigation area: A case study in Dongola, Sudan. *Energy Convers. Manag.* **2019**, *196*, 1453–1478. [CrossRef]
91. Zhang, L.; Barakat, G.; Yassine, A. Deterministic optimization and cost analysis of hybrid pv/wind/battery/diesel power system. *Int. J. Renew. Energy Res.* **2012**, *2*, 686–696.
92. Ma, T.; Javed, M.S. Integrated sizing of hybrid PV-wind-battery system for remote island considering the saturation of each renewable energy resource. *Energy Convers. Manag.* **2019**, *182*, 178–190. [CrossRef]
93. Suresh, V.; Muralidhar, M.; Kiranmayi, R. Modelling and optimization of an off-grid hybrid renewable energy system for electrification in a rural areas. *Energy Rep.* **2020**, *6*, 594–604. [CrossRef]
94. Tezer, T.; Yaman, R. Evaluation of approaches used for optimization of stand-alone hybrid renewable energy systems. *Renew. Sustain. Energy Rev.* **2017**, *73*, 840–853. [CrossRef]
95. Anoune, K.; Bouya, M.; Astito, A.; Abdellah, A.B. Sizing methods and optimization techniques for PV-wind based hybrid renewable energy system: A review. *Renew. Sustain. Energy Rev.* **2018**, *93*, 652–673. [CrossRef]
96. Alramlawi, M.; Gabash, A.; Mohagheghi, E.; Li, P. Optimal operation of hybrid PV-battery system considering grid scheduled blackouts and battery lifetime. *Sol. Energy* **2018**, *161*, 125–137. [CrossRef]
97. Nagapurkar, P.; Smith, J.D. Techno-economic optimization and social costs assessment of microgrid-conventional grid integration using genetic algorithm and Artificial Neural Networks: A case study for two US cities. *J. Clean Prod.* **2019**, *229*, 552–569. [CrossRef]
98. Das, M.; Singh, M.A.K.; Biswas, A. Techno-economic optimization of an off-grid hybrid renewable energy system using metaheuristic optimization approaches—Case of a radio transmitter station in India. *Energy Convers. Manag.* **2019**, *185*, 339–352. [CrossRef]
99. Akinsanola, A.A.; Ogunjobi, K.O.; Abolude, A.T.; Sarris, S.C.; Ladipo, K.O. Assessment of Wind Energy Potential for Small Communities in South-South Nigeria: Case Study of Koluama, Bayelsa State. *J. Fundam. Renew. Energy Appl.* **2017**, *7*, 1–6. [CrossRef]
100. Merem, E.C.; Twumasi, Y.; Wesley, J.; Alsarari, M.; Fageir, S.; Crisler, M.; Romorno, C.; Olagbegi, D.; Hines, A.; Ochai, G.S.; et al. Regional Assessment of Climate Change Hazards in Southern Nigeria with GIS. *J. Saf. Eng.* **2019**, *8*, 9–27. [CrossRef]
101. Okiongbo, K.S.; Douglas, R.K. Evaluation of major factors influencing the geochemistry of groundwater using graphical and multivariate statistical methods in Yenagoa city, Southern Nigeria. *Appl. Water Sci.* **2015**, *5*, 27–37. [CrossRef]
102. Lahimer, A.A.; Alghoul, M.A.; Yousif, F.; Razykov, T.M.; Amin, N.; Sopian, K. Research and development aspects on decentralized electrification options for rural household. *Renew. Sustain. Energy Rev.* **2013**, *24*, 314–324. [CrossRef]
103. NASA. Prediction of Worldwide Energy Resources. 2019. Available online: <https://power.larc.nasa.gov/> (accessed on 28 November 2020).
104. USGS. SRTM 30m Digital Elevation Data. Available online: <https://earthexplorer.usgs.gov/> (accessed on 20 September 2020).
105. FAO. Digital Soil Map of the World. Available online: <https://www.fao.org/land-water/land/land-governance/land-resources-planning-toolbox/category/details/en/c/1026564/> (accessed on 15 September 2020).
106. USGS. Landsat Mission Collection 7. Available online: <https://www.usgs.gov/landsat-missions/data> (accessed on 17 September 2020).
107. Kirke, B. Hydrokinetic and ultra-low head turbines in rivers: A reality check. *Energy Sustain. Dev.* **2019**, *52*, 1–10. [CrossRef]
108. Canadian Solar. MAXPOWER 325P Datasheet. Available online: <https://luisfgomez.com.do/wp-content/uploads/2017/10/Panel-Solar-Canadian-CS6U-315-330-Watts.pdf> (accessed on 5 January 2021).
109. Esan, A.B.; Agbetuyi, A.F.; Oghorada, O.; Ogbeide, K.; Awelewa, A.A.; Afolabi, A.E. Reliability assessments of an islanded hybrid PV-diesel-battery system for a typical rural community in Nigeria. *Heliyon* **2019**, *5*, e01632. [CrossRef]
110. EOCYCLE. Wind Turbine. 2020. Available online: <https://eocycle.com/our-wind-turbines/> (accessed on 1 May 2020).
111. Burwell, W.J. Optimizing and Implementing a Renewable Micro-Grid for a Remote Alaskan Village. Doctoral Dissertation, Harvard University, Ann Arbor, MI, USA, 2018.
112. Muratoglu, A.; Yuce, M.I. Design of a River Hydrokinetic Turbine Using Optimization and CFD Simulations. *J. Energy Eng.* **2017**, *143*, 04017009. [CrossRef]
113. Laws, N.D.; Epps, B.P. Hydrokinetic energy conversion: Technology, research, and outlook. *Renew. Sustain. Energy Rev.* **2016**, *57*, 1245–1259. [CrossRef]
114. Rolls, B.E. Battery Specification. Available online: https://www.rollsbattery.com/catalog/#renewable_energy (accessed on 18 December 2020).
115. Mongird, K.; Viswanathan, V.V.; Balducci, P.J.; Alam, M.J.E.; Fotedar, V.; Koritarov, V.S.; Hadjerioua, B. *Energy Storage Technology and Cost Characterization Report*; Department of Energy: Washington, DC, USA, 2019.
116. Leonics. Apollo MTP-410 Series Data Sheet—Three Phase Bidirectional Dual Mode Inverter for Mini-Grid System. Available online: <https://www.leonics.com/product/renewable/inverter/dl/MTP-410-091.pdf> (accessed on 14 November 2021).
117. Oladigbolu, J.O.; Ramli, M.A.M.; Al-turki, Y.A. Feasibility study and comparative analysis of hybrid renewable power system for off-grid rural electrification in a typical remote village located in Nigeria. *IEEE Access* **2020**, *8*, 171643–171663. [CrossRef]

118. CAT. Diesel Generator Set. Available online: https://cdn.shopify.com/s/files/1/0251/0215/5831/files/DE150E0-C_technical_offer.pdf?370 (accessed on 17 December 2021).
119. Ericson, S.; Olis, D. *A Comparison of Fuel Choice for Backup Generators*; NREL/TP-6A50-72509; National Renewable Energy Laboratory: Golden, CO, USA, 2019; p. 59.

Disclaimer/Publisher's Note: The statements, opinions and data contained in all publications are solely those of the individual author(s) and contributor(s) and not of MDPI and/or the editor(s). MDPI and/or the editor(s) disclaim responsibility for any injury to people or property resulting from any ideas, methods, instructions or products referred to in the content.